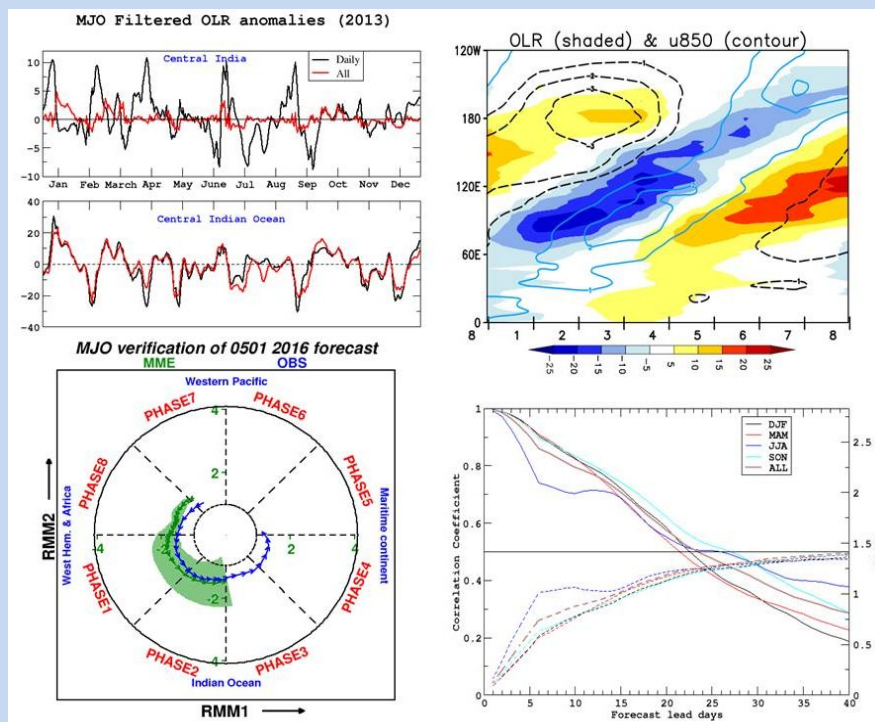


## MJO Diagnostics for Extended Range Prediction and Simulation in IITM CFSv2



Sahai A.K., Chattopadhyay Rajib, Dey Avijit, Joseph Susmitha, Abhilash S.,  
Phani M., Mandal Raju, Rajeevan M.N. and Hendon H.



Indian Institute of Tropical Meteorology (IITM)  
Earth System Science Organization (ESSO)  
Ministry of Earth Sciences (MoES)  
PUNE, INDIA  
<http://www.tropmet.res.in/>

ISSN 0252-1075  
Contribution from IITM  
Research Report No. RR-136  
*ESSO/IITM/SERP/SR/02(2016)/187*

## **MJO Diagnostics for Extended Range Prediction and Simulation in IITM CFSv2**

**Sahai A.K.<sup>1</sup>, Chattopadhyay Rajib<sup>1</sup>, Dey Avijit<sup>1</sup>, Joseph Susmitha<sup>1</sup>, Abhilash S.<sup>1</sup>,  
Phani M.<sup>1</sup>, Mandal Raju<sup>1</sup>, Rajeevan M.N.<sup>2</sup> and Hendon H<sup>3</sup>.**

<sup>1</sup> Indian Institute of Tropical Meteorology, Pune

<sup>2</sup> Ministry of Earth Sciences, New Delhi

<sup>3</sup> Bureau of Meteorology, Australia

**\*Corresponding Author Address:**

Dr. A.K. Sahai  
Indian Institute of Tropical Meteorology,  
Dr. Homi Bhabha Road, Pashan, Pune – 411 008, INDIA  
E-mail: sahai@tropmet.res.in  
Phone: +91-20-25904520



Indian Institute of Tropical Meteorology (IITM)

Earth System Science Organization (ESSO)

Ministry of Earth Sciences (MoES)

PUNE, INDIA

*<http://www.tropmet.res.in/>*

## DOCUMENT CONTROL SHEET

---

*Earth System Science Organization (ESSO)*  
*Ministry of Earth Sciences (MoES)*  
*Indian Institute of Tropical Meteorology (IITM)*

**ESSO Document Number**

ESSO/IITM/SERP/SR/02(2016)/187

**Title of the Report**

MJO Diagnostics for Extended Range Prediction and Simulation in IITM CFSv2

**Authors**

Sahai, A.K., Chattopadhyay, Rajib, Dey, Avijit, Joseph, Susmitha, S., Abhilash, M., Phani, Mandal, Raju, Rajeevan, M.N., Hendon, H.

**Type of Document**

Scientific Report (Research Report)

**Number of pages and figures**

69, 25

**Number of references**

67

**Keywords**

MJO diagnostics, EEOF, tracking & forecast, CFSv2, IITM-Extended range prediction system

**Security classification**

Open

**Distribution**

Unrestricted

**Date of Publication**

September, 2016

**Abstract**

A new method to track the smooth eastward propagation of Madden Julian Oscillation (MJO) is proposed in this report in order to use it for real-time prediction. The new method essentially removes any requirement of pre-filtering of data and is based on the extended empirical orthogonal function (EEOF) analysis of the zonal wind at 850hPa, 200hPa and the velocity potential ( $\chi$ ) at 200hPa. The lag used for creating the extended data matrix is 6 days (day 0 ...day 5). The EEOF method not only captures the MJO but also smooths the temporal propagation in the phase space defined by first two principal components (PCs) of the EEOFs. Along with traditional tracking in a phase space we extend the method to get the MJO-filtered spatial distribution of precipitation and other three dimensional variables associated with MJO. Examples of the TOGA-COARE and DYNAMO period are presented to compare the newly developed method with earlier ones.

## Contents

<b>1.</b>	<b>Introduction</b>	<b>1</b>
<b>2.</b>	<b>Data</b>	<b>4</b>
<b>3.</b>	<b>Model and Runs</b>	<b>4</b>
<b>4.</b>	<b>Methods</b>	
	4(a) The Wheeler and Hendon Method	6
	4(b) Standardization of indices	7
	4(c) Velocity potential as a replacement of OLR	7
	4(d) Spatial averaging	8
	4(e) Introducing time lag against filtering: tackling some real time tracking issues related to high frequency filtering.	9
	4(f) Seasonal variability of MJO and linking it with monsoon intraseasonal oscillation (MISO)	10
	4(g) Reconstruction of Variables (Rainfall/OLR etc.)	13
<b>5.</b>	<b>Application of the EEOF based technique: Results</b>	
	5(a) A comparison of tracking of MJO based on all methods	17
	5(b) Comparison of DYNAMO period	18
	5(c) MJO during 2015 summer monsoon season	19
	5(d) The TOGA-COARE (1992-93) period MJO	20
	5(e) Applying CFSv2 extended range forecast	21
<b>6.</b>	<b>Discussions and conclusions</b>	<b>23</b>
	<b>Acknowledgements</b>	<b>24</b>
	<b>References</b>	<b>25</b>
	<b>List of figures</b>	<b>30</b>
	<b>Figures</b>	<b>33</b>

# 1. Introduction

The Madden-Julian Oscillation (MJO) is the dominant mode of intraseasonal variability in the equatorial tropics (Madden and Julian 1972; Lau and Chan 1986; Hendon and Salby 1994; Madden and Julian 1994; Salby and Hendon 1994; Zhang 2005). It has a dominant periodicity in the range of 20-90 days and is traced to propagate eastward mostly originating from the Indian Ocean. The prediction of the initiation and the phase propagation of MJO remains a challenge to the operational forecasters as well as academic researchers (Zhang et al. 2013; Miyakawa et al. 2014; Ling et al. 2014). The impact of MJO is felt not only over the tropics but also over the extra-tropical region (Lau and Phillips 1986; Ferranti et al. 1990; Hsu 1996; Higgins and Mo 1997; Kim et al. 2006). Several studies have shown that predictive skill of MJO signal has significantly improved from earlier decades using general circulation model. However, representation of several features, as e.g. modulation of tropical cyclones by the MJO is not pretty good, even though the representation of convective variation and the modulation of tropical cyclone is well captured by dynamical models (Marshall et al. 2011; Vitart 2014; Neena et al. 2014b).

Some operational prediction centers (e.g. *CPC NCEP, USA, BoM, Australia*) regularly track and forecast the MJO year round. The operational tracking and forecasting of MJO is now standardized through a set of indices (Waliser et al. 2009; Gottschalck et al. 2010; Ventrice et al. 2013; Kiladis et al. 2014). Essentially the method, as described and proposed earlier in Wheeler and Hendon (2004), constructs a “phase plot” obtained based on scatter plots of 2 principal components derived from combined empirical orthogonal functions of meridionally averaged (15°S-15°N) outgoing longwave radiation (OLR) and zonal winds at 850hPa and 200hPa. Several variants of the same methods are also used routinely (Roundy and Schreck 2009; Kikuchi et al. 2012; Ventrice et al. 2013). Despite recent progress with

improving predictions of the MJO (Neena et al. 2014a) the physical origins of the MJO modes remain poorly understood. Multi-scale interactions and the role of synoptic “skeleton” have been emphasized in theoretical studies (Majda and Biello 2004; Shibagaki et al. 2006; Majda and Stechman 2009; Kikuchi and Wang 2010; Lau et al. 2012). Tropical-extratropical interactions are also known to influence the eastward propagation of convection associated with MJO (Lin et al. 2000; Ray and Zhang 2010). Thus several variables are used in order to capture different aspects of the MJO. In particular, recent approaches have used the velocity potential at 200hPa instead of OLR (Ventrice et al. 2013), which can help discriminate MJO events that have substantial amplitude outside of the tropical Indian Ocean - Western Pacific.

Owing to its influence on large scale circulations as well as regional weather, it is important to be able to monitor the MJO mode from operational analyses (also referred to as “observation” in the current study). MJO associated rainfall or the convective bands of clouds move systematically eastward producing regional increase in rainfall as well as exciting higher frequency regional weather patterns. Thus along with observational tracking, predicting these events in advance is also necessary. The clear eastward propagation and demarcation of tropical intraseasonal oscillations as an MJO event is especially prominent during the boreal winter season. The case during summer monsoon season is however quite debated in several studies. Although an eastward propagating component is still apparent, the boreal summer intraseasonal oscillation has a prominent northward propagating component into the Asian summer monsoon. It is argued by several studies that a fraction of the northward propagating components show eastward (Lawrence and Webster 2002), other studies claim that a large fraction of the monsoon intraseasonal oscillations are independent of the MJO during the boreal summer (Wang and Rui 1990; Jones et al. 2004).

The need to track the temporal evolution of the MJO and its role during the onset phase of Indian Summer Monsoon may also be demonstrated during monsoon onset in June (Mujumdar et al. 2015). June 2015 showed above normal rainfall over Indian region. During this period the northward propagation of convection became evident over the Indian region. Over the Pacific, the 2015 season showed strong signature of El-Nino. The eastward propagation of convection in June 2015 was difficult to assess due to the strong seasonally persisting convective anomalies associated with the El-Nino induced warming in the central Pacific. The purpose of this report is to develop a new approach to diagnosing the MJO that can be used for monitoring and assessment of predictions such as occurred during June 2015.

Requirements of the approach are:

- a. To propose an extended EOF based method that does not require temporal pre-filtering of the data.
- b. Small scale temporal and spatial variability (can be considered as noise in terms of MJO) are objectively filtered out from of the MJO pattern.
- c. Easy to use on dynamical model forecast interpretation in real-time.
- d. Can clarify the relationship between Monsoon Intraseasonal Oscillation (MISO) and MJO
- e. Obtain spatial distribution of rainfall (or any other field) associated with MJO.

We develop a variant of the diagnostic technique following a similar method as endorsed by MJO task force ([https://www.wmo.int/pages/prog/arep/wwrp/new/MJO\\_Task\\_Force\\_index.html](https://www.wmo.int/pages/prog/arep/wwrp/new/MJO_Task_Force_index.html)) with the ability to incorporate the same method in IITM CFSv2 extended range prediction system. The report will compare diagnostic techniques based on different methods and produce an updated framework for the diagnostic operational tracking as well as forecasting of rainfall.

The new method would not only provide an idea of propagation of the convection anomalies in a phase space but also provide the spatial distribution of MJO induced rainfall during the monsoon season.

## **2. Data**

The current report will demonstrate the description of the tracking method using observational analyses for the 1979-2009 periods. Recent years are excluded in order to use for independent verification purposes. The NCEP-NCAR reanalysis (Kalnay et al. 1996) are used for dynamic and thermo-dynamic fields, while IMD-TRMM merged gridded rainfall (Mitra et al. 2009) or TRMM data (Huffman et al. 2007) will be used for rainfall. For demonstration of case studies we chose the DYNAMO field campaign (Yoneyama et al. 2013; Zhang 2013) period (October-December 2011) and TOGA-COARE (Yanai et al. 2000; de Szoeke et al. 2014) period (November 1992–February 1993). During these two periods, several coordinated observation of MJO took place over the Indian Ocean and the MJO events are documented.

## **3. Model and Runs**

The main objective of this report is to use the MJO diagnostic technique to facilitate the comparison of Indian Institute of Tropical Meteorology (IITM), Pune CFSv2 extended range forecast with predictions from other global models. We use the latest version of NCEP CFSv2 (Saha et al. 2013) adopted at IITM as a model for *National Monsoon Mission, Govt. of India* (<http://www.tropmet.res.in/monsoon/>). The atmospheric component of the IITM CFSv2 model is NCEP Global Forecast System (GFS) at T126 (~100km) & T382 (~38km) resolution with 64 vertical levels, which is coupled to the ocean model, sea-ice model and land surface model. For its ocean component, the CFSv2 uses the GFDL Modular Ocean

Model version 4p0d (MOM4; Griffies et al. 2004) with zonal resolution of  $0.5^{\circ}$  and meridional resolution of  $0.25^{\circ}$  between  $10^{\circ}\text{S}$  and  $10^{\circ}\text{N}$ , gradually increasing through the tropics to  $0.5^{\circ}$  poleward of  $30^{\circ}\text{S}$  and  $30^{\circ}\text{N}$ . There are 40 layers in the vertical with 27 layers in the upper 400 m of the ocean, and the maximum depth is approximately 4.5 km. The vertical resolution is 10 m from the surface to 240 m depth, gradually increasing to about 511 m in the bottom layer. The initial conditions have been prepared from a weakly coupled data assimilation system (CDAS) with T574L64 resolution atmospheric assimilation and MOM4 based oceanic assimilation, and which is real-time extension of the CFSR (Saha et al. 2010).

The standalone GFS is forced with daily bias corrected forecasted SST from a single run of CFSv2 (BASE\_RUN). Bias correction of the BASE\_RUN is done by subtracting climatology of bias as a function of calendar day and lead time, with Optimally Interpolated SST (OISST) as the reference. We denote this forecast as GFSbc. For more model and experimental details and skills of GFSbc, CFST126 and CFST382, please refer (Abhilash et al. 2013), (Abhilash et al. 2014a), (Abhilash et al. 2014b) and (Sahai et al. 2014).

Based on the availability of computer resources for real time prediction we chose to run 11 ensemble members each of CFS (T126 & T382) and GFSbc (T126 & T382), so totally 44 ensemble forecasts are generated for next 45 days with every five days initial condition (IC) throughout the year. GFSbc runs use the bias corrected BASE\_RUN as boundary conditions as described in last paragraph. The ICs for the ensemble runs are created based on a perturbation technique as described in (Sahai et al. 2013; Abhilash et al. 2013). Finally a simple arithmetic averaging is done to get one single forecast (may be called as Multi-model Ensemble forecast, denoted as MME forecast) out of these 44 ensemble forecasts, since users want only one forecast that could be associated with confidence intervals.

## 4. Methods

### (a) The Wheeler and Hendon Method

The proposed method starts as an extension of the traditional Wheeler and Hendon (WH) method (Wheeler and Hendon 2004) based on empirical orthogonal function. In WH method, first the combined empirical orthogonal functions (EOF) of meridionally averaged ( $15^{\circ}\text{S}$ - $15^{\circ}\text{N}$ ) OLR, zonal winds at 850hPa and 200hPa are calculated after subtracting previous 120-day mean. The first two combined EOFs are diagnosed to be a pair (i.e. they explain similar variances and are correlated at lag of about 12 days) and are shown to represent the large scale components of the MJO mode (**Fig.1 of WH04**). Systematic evolution of the MJO is depicted by plotting phase-portrait of the first two principal components (PCs). The temporal power spectrum of PC1 and PC2 demonstrate peak power in the 20-90 day range (**Fig.1a**).

These 2 principal components are referred as the RMM indices. The RMM amplitude  $\sqrt{(\text{PC1}^2 + \text{PC2}^2)}$  and the location of the phase points for each day i.e. co-ordinates represented as [PC1, PC2] in the scatter plot (phase space) could be plotted as shown in **Fig.1b** to track the MJO mode. These phase-space plots of the RMM indices reveal more or less systematic unidirectional propagations (counterclockwise) showing tendency for systematic eastward propagation of the MJO with period near 40-50 days. Composite of any fields (e.g. precipitation) can be obtained first by equally (though arbitrarily) dividing the phase space into 8 equal segments (equivalent to Pizza-Slices) each sector spanning  $360^{\circ}/8=45^{\circ}$  angular space in the phase space (please refer **Fig.1b**) and then by collecting the days from each segments (terming them as each phase). The composites, thus obtained from eight phases for any fields would show systematic phase propagation reflecting the eastward propagation of convection. This is shown in **Fig.2**. Each of the eight phases (Phase1- phase 8) signifies a static location and the spatial structure of the convection band. A Hovmoller plot

from **Fig.2** could be obtained with meridional averaging between 15°S-15°N. This is shown in **Fig.3**. The clear eastward propagation of the convection band is evident in this plot. **Figure-1-3** forms the basis of the MJO diagnostic technique that forms the current standard. Several refinements of the same method are now being proposed to improve the phase space representation as well as the propagation of MJO. A few of them are discussed next.

### **(b) Standardization of indices**

The original WH method does not recommend any standardization of data at every grid point at the pre-processing stage, although it recommends to normalize each input field by its meridional mean standard deviation prior to computing EOF. It filters out interannual variability by subtraction of a 120-day mean but otherwise applies no other temporal filtering. However, standardized indices at every grid would be a useful way to track the result as the strength of MJO amplitudes as well as the EOFs would then be comparable in an easy way. The scaling of parameters are different in different levels, hence correlation matrix (instead of covariance matrix) might be good choice. The plot of the WH method based on a set of standardized input fields (OLR, U850, U200) are shown in **Fig.4-5**. The standardized anomalies used for creating the correlation/covariance matrix for EOF analysis are used as input instead of direct anomalies. It is clear that the phase propagation is comparable to the WH phase propagation. Recently, (Liu et al. 2015) has suggested an empirical global normalization value as opposed to what WH method has suggested. However, the choice looks somewhat arbitrary and is based on a few case studies. In this study we will take the grid-point normalization approach.

### **(c) Velocity potential as a replacement of OLR**

The OLR is a variable that reflects large scale convection and rainfall. Rainfall is ultimately the most important field that is required to be predicted. WH method recommends OLR as it

is easily available in near-real time for operational use. However, the rainfall-OLR relationship could be tricky at time especially over land. Also, over the western hemisphere the OLR based index could be problematic as the MJO signal in convection is weak. Ventrice et al.,(2013) noted “an improvement in some aspects of the RMM index when the OLR component of the index is replaced by 200-hPa velocity potential (VP200). In particular, differences were found in the representation of the MJO and its impacts over the Western Hemisphere.” They also noted that “Velocity potential is the inverse Laplacian of the divergence (Haltiner and Williams 1980). The inverse Laplacian acts an effective spatial-smoothing operator, so VP200 essentially describes the gravest planetary-scale characteristics of the upper-level divergence (Hendon 1986). OLR, in contrast, identifies the more regional characteristics of the divergence.” They provided a method in which OLR is replaced with VP200 in the method as described in Sec. 4a. They have also used some pre-filtering and normalization of the data. We reproduce the power spectra and the phase diagram based on the velocity potential index in **Fig.6a** and **Fig.6b** respectively. While the spatial propagation matches well with the RMM based method (**Fig.1a & Fig.2**) to a large extent as expected, the results indicate that large-scale field based metrics and indices could capture the spatio temporal information for MJO.

#### **(d) Spatial Averaging**

The discrimination to large-scale of variability as suggested by Ventrice et al., (2013) through the substitution of OLR with VP200 could be an effective way of smoothing out the small scale noise. Since the combined EOF analysis is at the heart of the technique, the spatial smoothing could additionally be achieved through averaging of grids. Averaging about the equator to remove small scale noise is at the heart of WH method. However, further smoothing in longitude could have additional benefits, including reducing the computational aspect. Also the post processed outputs of the model are derived in a variety of resolutions. In

order to bring an uniformity for MJO diagnostic purpose, in this report we propose that instead of using the usual  $2.5^{\circ} \times 2.5^{\circ}$  NCEP grid spacing (144 longitudes and 73 latitudes), we compute the combined EOFs of the fields by averaging the data in a  $10^{\circ}$  grid resolution along the longitude so that model forecast with a variety of resolutions versions can be directly compared with each other and also with observation. The large-grid scale assumption is also made to further filter out small-grid and spatially isolated systems (or regional high frequency standing waves) that could affect the MJO while propagating eastward. The Standardized indices are calculated on the spatially averaged data. Plots are shown in **Fig.7a** & **Fig.7b**. A comparison with the earlier figures **Fig.6a** & **Fig.6b** shows that the phase propagation is similar to a higher resolution result. Also the spectral peaks of PC1 and PC2 show comparable amplitude (i.e. variance) indicating nearly identical spectral resolution using both methods.

### **(e) Introducing time lag against filtering: tackling some real time tracking issues related to high frequency filtering**

The main downside of simple EOF analysis is that the input time series and the output principal components are affected by auto-correlation between the time series (Vanhatalo and Kulahci 2016). If the data contain multiple modes or periodicities as evident from the spectral plots of the field of interest and/or the scales are interacting with significant auto and cross-correlations in time, performing simple EOF or principal component analysis can be tricky (Huang 2010). Such noisy modes could be challenging if we want to compare the results between observation and models. For example, the projection of model data onto the observed EOF to get the PCs would also incorporate the noise structure embedded in the EOFs. These noise structures then are not only coming from model which is expected, but also coming from observation. Thus actual comparison in phase would incorporate additional

noise and could complicate the interpretation. The extended EOF (EEOF) approach is used in such situations for better noise reduction from observation, e.g. (Weare and Nasstrom 1982; Hannachi et al. 2007). The extended EOF method adds a time dimension to the vector being analyzed so that the temporal evolution is included when determining the principal modes of variation. EEOF analysis has the following advantages (i) more averaging is obtained in covariance matrix that implies smoother patterns and sometimes better signal to noise ratio, (ii) it contain lag-relationship information in the EEOF patterns and PC patterns that can help interpretation of the patterns. For intraseasonal oscillation this EEOF method have been applied earlier (Kikuchi et al. 2012). In this report we use the modifications as described in **Sec.4b-d** and after that we perform the extended EOF (EEOF) analysis by appending data up to six days in the covariance matrix to exclude the synoptic scale high frequency variability. The power spectra, phase plots and the Hovmoller diagram are shown in **Fig.8a, Fig.8b & Fig.9** respectively. In order to compare the phases of the current method and the RMM method so that optimum phase wise comparison can be made, we follow the method of Kiladis et al.,2014 (refer Table-2 of this paper) where the maximum correlation between daily PCs of the EEOF based method and RMM method are computed. Phases are constructed in such a way when the PCs of the EEOFs of our method and RMMs are maximum correlated. This removes the ambiguity of phasing and a one-to-one correspondence of RMM and EEOF based phases can be made. While the patterns in **Figs.8b-9** show similar eastward propagation, the phase plot looks much smoother. A comparison of model result and observation would be easier for smoothed patterns.

**(f) Seasonal variability of MJO and linking it with Monsoon Intra-Seasonal Oscillation (MISO)**

One of the common drawbacks of the MJO tracking method is the representation of MJO in boreal summer especially during the south Asian Summer Monsoon season over Indian Ocean is difficult. The indices those perform well to track the MJO during boreal winter could not be used with equal confidence during boreal summer. The convection associated with MJO mostly originates over the Indian Ocean. During the summer monsoon season over the Indian subcontinent, the northward propagation of the MISOs and the establishment of the land ITCZ in the backdrop of seasonal monsoon current make the distinction of MISO and MJO less clear. So far no single index is available that clearly separates MISO and MJO and brings the seasonal variability of the intraseasonal mode in a common tracking platform. WH also does a seasonally-dependent regression of any field onto the RMM indices and therefore can capture the clear distinction of mainly eastward propagation of the MJO in DJF and the eastward-poleward propagation during JJA.

A technique is developed and is reported here to overcome this inadequacy to study the MJO from observation and model simulation/prediction in which the effect of seasonal migration of ITCZ along with other dominant convective features are described in a uniform framework. This technique gives the position of the ITCZ and its seasonal oscillation above which the intraseasonal band is represented as northward and eastward propagating mode. The climatological or the canonical life-cycle of MJO is represented from the composite of days in each phase for any variable. For every day of a year, the phase location (i.e. the phase index ranging from Phase-1 to Phase 8) of the day itself, previous 45 days and the forward 45 days in the phase space is computed and saved. The same procedure is repeated and the phase index (locations) for the 365 days of all the years considered in the analysis is saved. Thus for any day, a composite anomaly could be made for every phase with the days having the same phase index number. The composite results for the day 15<sup>th</sup> January (**Fig.10.a** for OLR,

**Fig10.c** for Chi200 and **Fig.10.e** for precipitation) and the 15<sup>th</sup> July (**Fig.10.b** for OLR, **Fig10.d** for Chi200 and **Fig.10.f** for precipitation) cases are shown.

Two interesting results come out: *first*, all the plots show that for 15<sup>th</sup> January case there is a clear eastward propagation consistent with earlier studies those describe the canonical life-cycle of MJO. But the 15<sup>th</sup> July case shows both the eastward and northward propagation with the development of the land ITCZ consistent with the northward propagation of the phases of monsoon intraseasonal oscillations. Second, the phase orientation of the spatial pattern of MJO fields (Chi200) is oppositely inclined in boreal winter as compared to boreal summer. The seasonality of the Chi200 field associated with MJO is a new feature which would be explored more in future studies. To confirm that the eastward phase propagation of MJO and northward phase propagation of MISO (partly capturing MISO, but partly capturing MJO during NH summer when indeed it does propagate poleward) is correctly captured, we plot the Hovmoller propagations (averaged between 15°S-15°N for showing eastward propagation and averaged over 65°E-90°E for showing northward propagation) of the OLR, U850, vorticity at 850hpa & precipitation fields for 15<sup>th</sup> day of every month. Hovmoller plots for OLR (in  $W/m^2$ ; shaded) & U850 (contour, positive solid & negative dashed, contour interval 1 m/s) to show Eastward propagation are shown in **Figs.11**. It is clear from the figure that both low level zonal wind (U850) & OLR show clear eastward phase propagations during boreal winter. One important thing to be noted here that U850 field is leading OLR field. **Figs.12** shows Hovmoller plots for OLR (shaded) & relative vorticity at 850hPa (contour, positive solid & negative dashed, contour interval  $1 \times 10^{-6} s^{-1}$ ). Northward propagation of OLR and low level relative vorticity field are clear during boreal summer from **Figs.12**. Like eastward propagation (ref. **Figs.11**), it is to be noted that cyclonic (anticyclonic) vorticity at 850 hPa is to the north of the negative (positive) OLR anomalies as reported earlier (ref. Figs.2.15(a) of Goswami (2005)). These analyses support earlier results

that tropical intraseasonal low frequency oscillation (MJO & Boreal summer Intraseasonal Oscillation) evolves and sustains as a convectively coupled system. Hovmoller plots for precipitation are shown in **Figs.13-14**. It can be concluded from **Figs.11-14** that the eastward phase propagations are clear during boreal winter while the northward phase propagations are clear during boreal summer, reconfirming the conclusions of **Fig.10**. It is to be noted that the canonical life-cycle was created taking the indices (extended EOF analysis) of equatorial region spanning 15°S-15°N. Thus, the northward propagation of intraseasonal oscillation during the boreal summer could be obtained without any *a priori* assumption of monsoon intraseasonal oscillation. The consideration of seasonality, however, is known to improve MJO regression pattern as shown in (Jiang et al. 2008).

### **(g) Reconstruction of Variables (Rainfall/OLR etc.)**

The 2-dimensional (latitude  $\times$  longitude) reconstruction of rainfall associated with MJO is proposed in this study. This reconstruction would show the rainfall (convection) associated with the large-scale and low frequency component of MJO. The reconstruction of rainfall here is different than what is usual noise reduction reconstruction based on EOFs (Sahai et al. 2014). The reconstruction is based on reference location of a day in the [PC1, PC2] phase space. Any day in the phase space is characterized by the amplitude (“*amp*” as referred earlier) and its angular location in a particular *phase* (or “*pizza-slice*”). Each phase has a composite structure (spatial pattern) based on long-term averaging of data. The composite spatial pattern in each phase depends on the actual spatial resolution of the observation (or model output data) used for compositing and not on the input data matrix which is made low resolution.

Thus based on an EEOF of input data matrix with 10° longitudinal averaging, phase composites can be constructed by averaging the data on the days clustered in each phases as described in the previous paragraph.

Based on this composite structure and the relative location of this phase with respect to neighboring phases, *two methods* are proposed to reconstruct the spatial structure of rainfall associated with MJO for a day for any variable. We refer these methods as *phase index method* and *regression based method* respectively. They are described as follows:

**(I) Phase Index Method**

It consists of two basic steps:

**STEP A: Creation of composite anomalies**

In the first step calculations (i) to (iv) has to be done for any variable on the available grid resolution of the observed data.

(i) For smooth transition from one phase to another, phase space is divided into 40 equal parts (each separating 9 deg arc) instead of only eight phases that was done earlier.

(ii) Amplitude ( $\alpha = \sqrt{PC1^2 + PC2^2}$ ) and phase ( $\theta = \tan^{-1}(PC2/PC1)$ ) has been calculated for each day.

(iii) Scaled anomaly= (anomaly/ $\alpha$ ) has been calculated for all days when  $\alpha \geq 1.0$ .

(iv) Depending upon the  $\theta$  values for each day, composite anomalies for all the days in all the 40 phases were calculated from the scaled anomalies for each day (from 1 January to 31 December) using 45 previous and 45 forward days when  $\alpha \geq 1.0$ . These composite values are representative of the phase ( $\theta$  value) of the centre day of the 91 days considered. Such

running average composites are prepared for all the days in all the phases (each with angular width of 9°).

### **STEP B: Reconstruction of MJO filtered anomalies (*Ranom*)**

Once composite anomalies for each calendar day clustered in each of the 40 phases has been obtained for any variable as in **STEP A**, the following calculations has to be done for getting MJO filtered reconstructed anomalies for a particular day of a particular year:

(i) PC1 and PC2 have been calculated by projecting 10° longitudinal averaged & 15°S-15°N averaged standardized anomaly values of VP200, U200 and U850.

(ii)  $\alpha$  and  $\theta$  have been calculated as (ii) of STEP A

(iii) Angular distance  $\theta_i$  and  $\theta_{i+1}$  has been calculated from the nearest two neighboring phases (**i** and **i+1**) out of 40 phases. Let  $C_i$  and  $C_{i+1}$  be the scaled composite anomalies of respective phases. Then the MJO filtered reconstructed anomalies can be written as

$$\mathbf{Ranom} = \alpha * (C_i * \theta_{i+1} + C_{i+1} * \theta_i) / (\theta_i + \theta_{i+1})$$

The above methods of reconstruction have following advantages:

- i. It can be used for any variables to get the MJO filtered spatial pattern or the full 3 dimensional structure of a field whose composites are available (as in Step-A).
- ii. It can be applied in real-time applications as it does not involve filtering.
- iii. The reconstruction is independent of spatial resolution of the data used as input to EEOF analysis. For example, reconstruction of precipitation data could be made at high resolution TRMM or GPM data even though the EEOFs are calculated based on averaged quantities in which rainfall is not used.

The new reconstruction method shows several important improvements in terms of filtering the summer time intraseasonal oscillation. The example is shown in **Fig.15**, where plots of reconstructed OLR over central Indian land region (70-85E, 20-28N) and central Indian Ocean region (70°-85°E, 5°S-5°N) for the year 2013 based on lagged phase composite method (-45 day to +45 day), it takes seasonality into account and simple phase composite method (considering all the days of the year), are shown. While over Indian Ocean region both methods show identical temporal evolution during all the months of 2013, over Indian land region the lagged method shows significant improvement (the intraseasonal oscillation during the monsoon season is clear over Indian land). Thus using the lagged reconstruction of composites, we find that the index of MJO and MISO could be represented in a dual mode. Thus, the technique is able to demonstrate the link between MJO and MISO. This will be reported further in future studies. The direct application of WH type RMM method could not reflect it (e.g. Fig.12 of (Suhas et al. 2012)) although time-lagged regression of WH method could reflect this as argued in (Jiang et al. 2008).

Further examples of rainfall reconstruction during the DYNAMO period and TOGA-COARE period will be shown in **Sec.5**.

### ***(II) Regression Based Method***

In this method the PC1 and PC2 indices are used to regress any variable to be reconstructed at each grid point. We have used a 45 day lagged vector of PC1 and PC2 in this reconstruction to incorporate the seasonality of the coefficients as discussed in previous section. Based on a history of past data, a variable (e.g. OLR at location  $(x,y)$  and time  $t$ ) is reconstructed as :

$$OLR(x, y, yr, t) = B0(x, y, t) + B1(x, y, t) * PC1(yr, t) + B2(x, y, t) * PC2(yr, t)$$

Where  $t$  is the current day to be reconstructed ( $t=1\dots365$ ),  $B_0$ ,  $B_1$  and  $B_2$  are the regression coefficients for each of the 365 days of a year to be determined based on a pull of past data.

The phase index method (method (I)) has the ambiguity that the reconstruction is dependent on the number of phases those have to be empirically predefined. The regression based method does not suffer from this restriction. Hence, though both the methods give qualitatively similar results (cf. Sec.5d), it is advantageous to use regression based method. It is to be noted that this reconstruction can equally be done using RMM method.

## **5. Applications of the EEOF based technique: Results**

### **(a) A comparison of tracking of MJO based on all methods**

In order to gain an understanding of the performance improvements of all the methods discussed in Sec.4, we first show the tracking of MJO during the September to December period (SOND) of 2009 (year chosen arbitrarily). The phase diagrams are shown for the conventional Wheeler and Hendon 2004 (WH) method (**Fig.16.a**); standardization of indices method as discussed in Sec.4b (**Fig.16.b**); Velocity potential as a replacement of OLR as discussed in Sec.4c (**Fig.16.c**); Spatial averaging method as discussed in Sec. 4d (**Fig.16.d**); and EEOF analysis technique as discussed in Sec.4e (**Fig.16.e**). The figure clearly shows that with spatial averaging and using the EEOF analysis, the smoothing of the MJO track is obtained with better fidelity. The purpose of this plot is to show how smoothing is achieved with the current proposed method. However, whether the smoothing has made the MJO tracking more realistic or not, is not evident. It could be easily seen that the amplitudes are quite different with the phase propagation are quantitatively dissimilar. In order to see this, we next discuss the results based on the proposed method and earlier methods for the CINDY-DYNAMO period (Zhang 2013) in next section.

## (b) Comparison of DYNAMO period

The DYNAMO field campaign (Zhang 2013) conducted during October-December of 2011 provided an opportunity to validate the technique developed as above. Two major (strong) MJOs were reported during the October to December 2011, they are referred as MJO1 and MJO2 in earlier studies (Yoneyama et al. 2013; Kiladis et al. 2014). The hovmoller plot for OLR during this period is shown in **Fig.17.a**. This plot is shown in Kiladis et al., (2014). The **Fig.17.a** shows raw OLR anomaly (shaded) with the 20-90 day Lanczos filtered anomaly component (contours) superimposed on it to highlight the MJO component. **Fig.17b** shows the reconstructed OLR anomaly (shaded) from the current technique with the 20-90 day Lanczos filtered anomaly component (contours) superimposed on it. The comparison clearly demonstrates the fidelity of the reconstruction based on our current technique.

The tracking of MJO based on our method and a comparison of the previously existing methods (refer Sec.4a-c) is given in **Fig.18**. It is clear that a smooth MJO propagation is seen during the MJO1 and MJO2 period. The shortcoming of the RMM based method is discussed in Kiladis et al., 2014. It is clear from a comparison of MJO1 and MJO2 based on **Fig.18** that the current method (**Fig.18.b**) gives the peak amplitude of MJO1 at a proper time (around 25<sup>th</sup> October, in Phase 2), which RMM method (**Fig.18.a**) can't give as discussed in Kiladis et al.,(2014). Kiladis et al.,(2014) showed that the "OMI" and the "FMO" indices capture the MJO1 initiation quite well. Kiladis et al,(2014) also commented that the second MJO (MJO2) amplitude was quite erratic and sharply peaked in OMI and FMO indices while a strong amplitude of MJO based on RMM index is visible in the phase plot (Phase 4-5). Thus, RMM method has difficulty in capturing initiation stages of MJO1 but performed better in capturing MJO2; while RMM method capture MJO2 over Phase 4-5, which the OMI and FMO indices can't. The reason of this discrepancy could be due to the fact that MJO is both dynamical and

convectively evolving with time and usage of a dynamical and/or convective parameter in principal component analysis technique could reflect this ambiguity. The plot from the current technique as reported here however shows that both MJO1 and MJO2 events are captured at the right time steps as described earlier. Thus, the current EEOF based method shows improvement over the past existing techniques. The improvement shows that essentially EEOF techniques has the effect of bandpass or high pass filtering through use of multiple time lags in the covariance/correlation matrix.

### (c) MJO during 2015 summer monsoon season

The summer monsoon season of 2015 is a deficient year (86% of long-period-average). However, the June 2015 was an excess month with signals of MJO can be seen propagating eastward. Several studies have shown relationship of MJO with active and break spells of Indian summer monsoon intraseasonal oscillations (Saith and Slingo 2006; Joseph et al. 2009; Pai et al. 2009). The tracking of MJO during the boreal summer 2015 monsoon season is shown following WH method (**Fig.19.a**) and current EEOF analysis technique (**Fig.19.b**). During June, the Western Indian Ocean and western Pacific including maritime continent was having the signature of strong amplitude MJO. Under such conditions strong convective anomalies were seen over Indian landmass. Although the link of monsoon intraseasonal oscillation with eastward propagation of convection is not very clear during June 2015, an association of active condition was claimed in earlier studies (Pai et al. 2009). Such associations are required to be investigated further. The 2015 is a strong ENSO year and naturally the conditions in the central and east Pacific were always having warm SST anomalies. Such seasonally strong and persisting anomalies of SST and associated convection over the equatorial Pacific would indicate that the propagation of MJO could get hampered as seen in the phase plot of July, August and September. For a long period of time the MJO is

seen to be unusually pulsating in Phase 7-8 indicating a possible role of ENSO basic state. This requires further investigation and will be addressed in future work.

#### (d) The TOGA-COARE (1992-93) period MJO

As a final case to report here, we discuss the TOGA-COARE period MJO (Yanai et al. 2000; de Szoeke et al. 2014) as recently reviewed by Liu et al (2015). Yanai et al., (2000) suggested that during the TOGA COARE period (November 1992–February 1993), two distinct MJO events propagated those were associated with super cloud clusters and westerly wind bursts. Liu et al.(2015) analyzed these two events based on the traditional RMM (1&2) indices and a newly defined “*revised RMM index*” (RMM-r) method that uses a new normalization value of the covariance matrix. In **Fig.20** we revisit the results for the two MJO events during TOGA COARE observation period. **Fig.20a** shows the plot for unfiltered (i.e. actual) OLR anomaly (from climatology) and wavenumber frequency filtered OLR during the DJF period (December to February) of 1992-93. The wavenumber frequency filtering was done by retaining wavenumbers 1-5 and frequency 20-100 day similar to that used in Liu et al., (2015), which is based on the 2-D spectral filtering method (e.g. Wheeler and Kiladis(1999)). **Fig.20b** shows the reconstructed MJO using the currently developed *Phase Index* method (shaded) and is compared with the wavenumber frequency filtered OLR (contours). The reconstruction based on *phase Index* method is shown in **Fig.20b** (shaded) and the *regression based method* is shown in **Fig.20d** (shaded). Contours of MJO filtered anomalies created with traditional wave-frequency filtering method are also superimposed on both the plots. The plot clearly shows that the two MJO events are captured by the two reconstruction methods. The two reconstruction methods will be used in future for further analysis. The *phase index* method, does not involve any linearity assumption as required by the linear *regression based method*. Since both the methods show similar results for this TOGA COARE case, the

simpler linear *regression method* is recommended. However, further analysis is required in this direction based on many more cases to confirm the merits of reconstruction based on any of these methods.

A comparison of **Fig.20b** with the results of Liu et al., (2015) shows quite similarity in the reconstructed MJO based on two techniques. There is, however, one important difference with the amplitude based on the reconstruction of *Liu et al., (2015)* and the newly defined *Phase Index method*, as can be seen in **Fig.20c**. The first MJO is a weak MJO if defined based on RMM index or the *Phase Index (RMM\_L)* method. The amplitudes for these two methods never touched 1 unit along abscissa. This is not the case with Liu et al., (2015) (refer *Figure 5* of the paper) which has cross 1 around 21 December. Thus, Liu et al., (2015) declares it a strong MJO which is not so based on RMM or the newly developed method described here based on *Phase Index method (RMM\_L)*. The reason of this discrepancy needs further analysis which is not attempted here. The corresponding phase monitoring is shown in **Fig.21** which compares well with the earlier methods. **Fig.22a-b** shows the same plot as the **Fig.20a-b** but for velocity potential at 200hPa (chi200). The plots in both these figures are consistent implying that the reconstructions of MJO filtered anomalies are comparable with wavenumber-frequency filtering methods.

### (e) Applying CFSv2 extended range forecast

The bivariate correlation and root mean square error is a standard method to estimate the skill of dynamical models (Rashid et al. 2010; Kim et al. 2014). Following Rashid et al., (2010) we define bivariate correlation at a lead time  $\tau$  as:

$$cc(\tau) = \frac{\sum_{t=1}^N [a1(t)b1(t, \tau) + a2(t)b2(t, \tau)]}{\sqrt{\sum_{t=1}^N [a1^2(t) + a2^2(t)]} \sqrt{\sum_{t=1}^N [b1^2(t, \tau) + b2^2(t, \tau)']}}$$

$$RMSE(\tau) = \sqrt{\frac{1}{N} \sum_{t=1}^N [(a1(t) - b1(t, \tau))^2 + (a2(t) - b2(t, \tau))^2]}$$

Here,  $a_1(t)$  and  $a_2(t)$  are the verification PC1 and PC2 at time  $t$ , and  $b_1(t, \tau)$  and  $b_2(t, \tau)$  are the respective forecasts for time  $t$  for a lead time of  $\tau$  days.  $N$  is the number of forecasts.

$b_1$  and  $b_2$  are computed based on projection of real-time data onto the EEOFs (EEOFs are extended up to lag -5 from lag 0). Since it is difficult to get near real-time observation data of all variables required to project onto the EEOFs to calculate the real-time PCs from any initial condition, we have used the previous (5 days back) forecast data for the first five day forecast to create the covariance matrix.

The **Fig.23** is plotted to estimate the season wise statistical skill of the model during 2001-2010 CFSv2 extended range hindcast period. The skill for the first five day could be ignored as it contains the artificial information from last forecasts as discussed in last paragraph. The skills of the model forecasts during all the seasons are almost similar with the skills extending up to 25 days or more for all the seasons. This skill may be compared with the results of (Miyakawa et al. 2014; Ling et al. 2014) who has reported similar skill with the ECMWF and NICAM hindcast runs.

As an example to demonstrate the performance of the model we provide a real-time example of the May 2016 case when an eastward propagation of a fairly strong MJO is seen in phase space (**Fig.24**). Since this MJO also originated during the onset phase of monsoon it is interesting to track the same based on the IITM extended range prediction system. The tracking of the same MJO in phase space is shown in different panels of Fig.24(a-e). The initial conditions (date) are mentioned in the top of different panels. The forecast from different initial conditions indicate that the MJO was well forecasted since the end of April

2016 ICs. Fig.24(f) phase space plot of RMM index (obtained from Bureau of Meteorology) for MAY 2016. Further evaluation of the skill of MJO forecasts for different events is under process.

## 6. Discussions and Conclusions

The aim of the current report is to document a comprehensive framework for the diagnosis of MJO from observation primarily to benefit the extended range prediction system. Observation based state-of-art MJO diagnostics is reproduced here with an additional proposition of an EEOF based analysis. The EEOF based analysis makes phase trajectories relatively smoother (i.e. filtering out undesired modes) than previous techniques. The purpose of this smoothing is to make the phase tracking more easily comparable with model outputs from extended range prediction system. The results during the DYNAMO period, TOGA-COARE period and the 2015 and 2016 MJO events during monsoon time are produced here to compare with each other and with earlier methods. Additionally, the method is extended to extract the spatial as well as full 3 dimensional structure of MJO associated variables (i.e. a type of space-time filtered pattern of MJO) based on phase-space method and regression based method. The regression based method could be used more efficiently to reconstruct the MJO filtered fields. The reconstructed structure of rainfall or any other variable could be used for real-time comparison with any forecast model output. As an example to show the efficiency of this reconstruction method, we plot the actual and reconstructed OLR in **Fig. 25**. It may be easily seen that the reconstructed OLR based on regression based method has filtered out the undesired modes (Rossby/Kelvin waves etc.), thus bringing out the smoother trajectories in earlier plots.

The EEOF based analysis also takes into account the boreal summer mode which is represented correctly with proper positioning of ITCZ over the ocean and the land. A

uniform framework is proposed to get the boreal summer intraseasonal oscillation mode. The results show that the life cycle of MJO and the summer intraseasonal oscillations could be captured with equal fidelity using this method.

Thus, in brief, the main advantages of the proposed EEOF based system are: (a) smoother propagation of convection associated with MJO, which would be useful for real-time applications, (b) pre-filtering of data is kept to minimum and yet tracks of smooth MJO propagation could be obtained. This method could be directly used for comparison of model forecast, (c) MJO filtering could be done for any space-time data and not *only* with the variable used in filtering, (d) long model integrations are not required for tracking the model generated MJO and (e) MJO and the boreal summer intraseasonal oscillations could be treated with a uniform framework. The proposed framework (**Sec.4e-f**) would be used for comparison of the IITM extended range forecast system for future use.

## **Acknowledgments**

IITM is fully supported by Ministry of Earth Sciences, Govt. of India, New Delhi, India.

## References

- Abhilash, S., A. K. Sahai, S. Pattnaik, and S. De, 2013: Predictability during active break phases of Indian summer monsoon in an ensemble prediction system using climate forecast system. *Journal of Atmospheric and Solar-Terrestrial Physics*, **100–101**, 13–23, doi:10.1016/j.jastp.2013.03.017.
- Abhilash, S., and Coauthors, 2014a: Prediction and monitoring of monsoon intraseasonal oscillations over Indian monsoon region in an ensemble prediction system using CFSv2. *Clim Dyn*, **42**, 2801–2815, doi:10.1007/s00382-013-2045-9.
- , A. K. Sahai, S. Pattnaik, B. N. Goswami, and A. Kumar, 2014b: Extended range prediction of active-break spells of Indian summer monsoon rainfall using an ensemble prediction system in NCEP Climate Forecast System. *Int. J. Climatol.*, **34**, 98–113, doi:10.1002/joc.3668.
- Ferranti, L., T. N. Palmer, F. Molteni, and E. Klinker, 1990: Tropical-Extratropical Interaction Associated with the 30–60 Day Oscillation and Its Impact on Medium and Extended Range Prediction. *Journal of the Atmospheric Sciences*, **47**, 2177–2199, doi:10.1175/1520-0469(1990)047<2177:TEIAWT>2.0.CO;2.
- Goswami, B. N. (2005). South Asian Monsoon (chapter 2): Intraseasonal Variability in the Atmosphere-Ocean Climate System, William K. M. Lau & Duane E. Waliser (Eds.). Chichester, UK: Springer Praxis Publishing, pp. 19-54
- Gottschalck, J., and Coauthors, 2010: A Framework for Assessing Operational Madden–Julian Oscillation Forecasts: A CLIVAR MJO Working Group Project. *Bulletin of the American Meteorological Society*, **91**, 1247–1258, doi:10.1175/2010BAMS2816.1.
- Griffies, Stephen M., Matthew J. Harrison, Ronald C. Pacanowski and Anthony Rosati, 2004, A Technical Guide to MOM4, GFDL Ocean Group Technical Report No. 5, Princeton, NJ, NOAA/Geophysical Fluid Dynamics Laboratory, 342 pp.
- Haltiner, G. J., and R. T. Williams, 1980: *Numerical Prediction and Dynamic Meteorology*. John Wiley and Sons, 477 pp.
- Hannachi, A., I. T. Jolliffe, and D. B. Stephenson, 2007: Empirical orthogonal functions and related techniques in atmospheric science: A review. *International Journal of Climatology*, **27**, 1119–1152, doi:10.1002/joc.1499.
- Hendon, H. H., 1986: Streamfunction and Velocity Potential Representation of Equatorially Trapped Waves. *J. Atmos. Sci.*, **43**, 3038–3042, doi:10.1175/1520-0469(1986)043<3038:SAVPRO>2.0.CO;2.
- Hendon, H. H., and M. L. Salby, 1994: The life cycle of the Madden–Julian oscillation. *J. Atmos. Sci.*, **51**, 2225–2237.
- Higgins, R. W., and K. C. Mo, 1997: Persistent North Pacific Circulation Anomalies and the Tropical Intraseasonal Oscillation. *J. Climate*, **10**, 223–244, doi:10.1175/1520-0442(1997)010<0223:PNPCAA>2.0.CO;2.
- Hsu, H.-H., 1996: Global View of the intraseasonal Oscillation during Northern Winter. *J. Climate*, **9**, 2386–2406, doi:10.1175/1520-0442(1996)009<2386:GVOTIO>2.0.CO;2.

- Huang, X., 2010: Topics in Multivariate Time Series Analysis: Statistical Control, Dimension Reduction Visualization and Their Business Applications. *Dissertations*,. [http://scholarworks.umass.edu/open\\_access\\_dissertations/204](http://scholarworks.umass.edu/open_access_dissertations/204).
- Huffman, G. J., and Coauthors, 2007: The TRMM Multisatellite Precipitation Analysis (TMPA): Quasi-Global, Multiyear, Combined-Sensor Precipitation Estimates at Fine Scales. *Journal of Hydrometeorology*, **8**, 38–55, doi:10.1175/JHM560.1.
- Jiang, X., D. E. Waliser, M. C. Wheeler, C. Jones, M.-I. Lee, and S. D. Schubert, 2008: Assessing the Skill of an All-Season Statistical Forecast Model for the Madden–Julian Oscillation. *Mon. Wea. Rev.*, **136**, 1940–1956, doi:10.1175/2007MWR2305.1.
- Jones, C., L. M. V. Carvalho, R. Wayne Higgins, D. E. Waliser, and J.-K. E. Schemm, 2004: Climatology of Tropical Intraseasonal Convective Anomalies: 1979–2002. *J. Climate*, **17**, 523–539, doi:10.1175/1520-0442(2004)017<0523:COTICA>2.0.CO;2.
- Joseph, S., A. K. Sahai, and B. N. Goswami, 2009: Eastward propagating MJO during boreal summer and Indian monsoon droughts. *Clim Dyn*, **32**, 1139–1153, doi:10.1007/s00382-008-0412-8.
- Kalnay E, Kanamitsu M, Kistler R, et al (1996) The NCEP/NCAR 40-Year Reanalysis Project. *Bulletin of the American Meteorological Society* 77:437–471. doi: 10.1175/1520-0477(1996)077<0437:TNYRP>2.0.CO;2
- Kikuchi, K., and B. Wang, 2010: Spatiotemporal Wavelet Transform and the Multiscale Behavior of the Madden–Julian Oscillation. *J. Climate*, **23**, 3814–3834.
- Kikuchi, K., B. Wang, and Y. Kajikawa, 2012: Bimodal representation of the tropical intraseasonal oscillation. *Climate Dynamics*, **38**, 1989–2000, doi:10.1007/s00382-011-1159-1.
- Kiladis, G. N., J. Dias, K. H. Straub, M. C. Wheeler, S. N. Tulich, K. Kikuchi, K. M. Weickmann, and M. J. Ventrice, 2014: A Comparison of OLR and Circulation-Based Indices for Tracking the MJO. *Mon. Wea. Rev.*, **142**, 1697–1715, doi:10.1175/MWR-D-13-00301.1.
- Kim, B.-M., G.-H. Lim, and K.-Y. Kim, 2006: A new look at the midlatitude–MJO teleconnection in the northern hemisphere winter. *Q.J.R. Meteorol. Soc.*, **132**, 485–503, doi:10.1256/qj.04.87.
- Kim, H.-M., P. J. Webster, V. E. Toma, and D. Kim, 2014: Predictability and Prediction Skill of the MJO in Two Operational Forecasting Systems. *J. Climate*, **27**, 5364–5378, doi:10.1175/JCLI-D-13-00480.1.
- Lau, D. W. K. M., D. D. E. Waliser, A. J. Majda, and S. N. Stechmann, 2012: Multiscale theories for the MJO. *Intraseasonal Variability in the Atmosphere-Ocean Climate System*, Springer Praxis Books, Springer Berlin Heidelberg, 549–568 [http://link.springer.com/chapter/10.1007/978-3-642-13914-7\\_17](http://link.springer.com/chapter/10.1007/978-3-642-13914-7_17) (Accessed May 13, 2013).
- Lau, K. M., and P. H. Chan, 1986: Aspects of the 40-50 day oscillation during the northern summer as inferred from outgoing longwave radiation. *Mon. Wea. Rev.*, **114**, 1354–1367.
- , and T. J. Phillips, 1986: Coherent fluctuations of extratropical geopotential height and tropical convection in intraseasonal time scales. *J. Atmos. Sci.*, **43**, 1164–1181.
- Lawrence, D. M., and P. J. Webster, 2002: The Boreal Summer Intraseasonal Oscillation: Relationship between Northward and Eastward Movement of Convection. *J. Atmos. Sci.*, **59**, 1593–1606, doi:10.1175/1520-0469(2002)059<1593:TBSIOR>2.0.CO;2.

- Lin, J. W.-B., J. D. Neelin, and N. Zeng, 2000: Maintenance of Tropical Intraseasonal Variability: Impact of Evaporation–Wind Feedback and Midlatitude Storms. *J. Atmos. Sci.*, **57**, 2793–2823, doi:10.1175/1520-0469(2000)057<2793:MOTIVI>2.0.CO;2.
- Ling, J., P. Bauer, P. Bechtold, A. Beljaars, R. Forbes, F. Vitart, M. Ulate, and C. Zhang, 2014: Global versus Local MJO Forecast Skill of the ECMWF Model during DYNAMO. *Mon. Wea. Rev.*, **142**, 2228–2247, doi:10.1175/MWR-D-13-00292.1.
- Liu, P., Q. Zhang, C. Zhang, Y. Zhu, M. Khairoutdinov, H.-M. Kim, C. Schumacher, and M. Zhang, 2015: A Revised Real-Time Multivariate MJO Index. *Mon. Wea. Rev.*, **144**, 627–642, doi:10.1175/MWR-D-15-0237.1.
- Madden, R., and P. Julian, 1972: Description of global scale circulation cells in the Tropics with a 40–50 day period. *J. Atmos. Sci.*, **29**, 1109–1123.
- Madden, R. A., and P. R. Julian, 1994: Observations of the 40-50-Day Tropical Oscillation - a Review. *Mon. Wea. Rev.*, **122**, 814–837.
- Majda, A. J., and J. A. Biello, 2004: A multiscale model for tropical intraseasonal oscillation. *Proc. Natl. Acad. Sci.*, **101**, 4736–4741.
- Majda, A. J., and S. N. Stechman, 2009: The skeleton of tropical intraseasonal oscillations. *Proc. Natl. Acad. Sci.*, **106**, 8417–8422.
- Marshall, A. J., D. Hudson, M. C. Wheeler, H. H. Hendon, and O. Alves, 2011: Assessing the simulation and prediction of rainfall associated with the MJO in the POAMA seasonal forecast system. *Climate Dynamics*, **37**, 2129–2141, doi:10.1007/s00382-010-0948-2.
- Mitra, A. K., A. K. Bohra, M. N. Rajeevan, and T. N. Krishnamurti, 2009: Daily Indian Precipitation Analysis Formed from a Merge of Rain-Gauge Data with the TRMM TMPA Satellite-Derived Rainfall Estimates. *Journal of the Meteorological Society of Japan. Ser. II*, **87A**, 265–279.
- Miyakawa, T., and Coauthors, 2014: Madden–Julian Oscillation prediction skill of a new-generation global model demonstrated using a supercomputer. *Nat Commun*, **5**, 3769, doi:10.1038/ncomms4769.
- Mujumdar, M., C. Gnanseelan, and M. N. (Edited. Rajeevan, 2015: *A Research Report on the 2015 Southwest Monsoon*. ESSO-IITM, Pune, <http://www.tropmet.res.in/~lip/Publication/Scientific-Reports/RR-185.pdf>.
- Neena, J. M., J. Y. Lee, D. Waliser, B. Wang and X. Jiang, 2014a: Predictability of the Madden Julian oscillation in the Intra-seasonal Variability Hindcast Experiment (ISVHE). *J. Climate*, **27**, 4531–4543, doi:10.1175/JCLI-D-13-00624.1
- , X. Jiang, D. Waliser, J.-Y. Lee, and B. Wang, 2014b: Eastern Pacific Intraseasonal Variability: A Predictability Perspective. *J. Climate*, **27**, 8869–8883, doi:10.1175/JCLI-D-14-00336.1.
- Pai, D. S., J. Bhate, O. P. Sreejith, and H. R. Hatwar, 2009: Impact of MJO on the intraseasonal variation of summer monsoon rainfall over India. *Clim Dyn*, **36**, 41–55, doi:10.1007/s00382-009-0634-4.
- Rashid, H. A., H. H. Hendon, M. C. Wheeler, and O. Alves, 2010: Prediction of the Madden–Julian oscillation with the POAMA dynamical prediction system. *Clim Dyn*, **36**, 649–661, doi:10.1007/s00382-010-0754-x.

- Ray, P., and C. Zhang, 2010: A Case Study of the Mechanics of Extratropical Influence on the Initiation of the Madden–Julian Oscillation. *J. Atmos. Sci.*, **67**, 515–528, doi:10.1175/2009JAS3059.1.
- Roundy, P. E., and C. J. Schreck, 2009: A combined wave-number–frequency and time-extended EOF approach for tracking the progress of modes of large-scale organized tropical convection. *Quart. J. Roy. Meteor. Soc.*, **135**, 161–173.
- Saha, S., and Coauthors, 2010: The NCEP Climate Forecast System Reanalysis. *Bull. Amer. Meteor. Soc.*, **91**, 1015–1057, doi:10.1175/2010BAMS3001.1.
- , and Coauthors, 2013: The NCEP Climate Forecast System Version 2. *J. Climate*, **27**, 2185–2208, doi:10.1175/JCLI-D-12-00823.1.
- Sahai, A. K., and Coauthors, 2013: Simulation and Extended range prediction of Monsoon Intraseasonal Oscillations in NCEP CFS/GFS version 2 framework. *Curr. Sci.*, **104**, 1394–1408.
- , R. Chattopadhyay, S. Joseph, S. Abhilash, N. Borah, and B. N. Goswami, 2014: A new method to compute the principal components from self-organizing maps: an application to monsoon intraseasonal oscillations. *Int. J. Climatol.*, **34**, 2925–2939, doi:10.1002/joc.3885.
- Saith, N., and J. Slingo, 2006: The role of the Madden–Julian Oscillation in the El Niño and Indian drought of 2002. *Int. J. Climatol.*, **26**, 1361–1378, doi:10.1002/joc.1317.
- Salby, M. L., and H. H. Hendon, 1994: Intraseasonal Behavior of Clouds, Temperature, and Motion in the Tropics. *J. Atmos. Sci.*, **51**, 2207–2224, doi:10.1175/1520-0469(1994)051<2207:IBOCTA>2.0.CO;2.
- Shibagaki, Y., and Coauthors, 2006: Multiscale Aspects of Convective Systems Associated with an Intraseasonal Oscillation over the Indonesian Maritime Continent. *Mon. Wea. Rev.*, **134**, 1682–1696, doi:10.1175/MWR3152.1.
- Suhas, E., J. Neena, and B. Goswami, 2012: An Indian monsoon intraseasonal oscillations (MISO) index for real time monitoring and forecast verification. *Climate Dynamics*, 1–12, doi:10.1007/s00382-012-1462-5.
- de Szoek, S. P., J. B. Edson, J. R. Marion, C. W. Fairall, and L. Bariteau, 2014: The MJO and Air–Sea Interaction in TOGA COARE and DYNAMO. *J. Climate*, **28**, 597–622, doi:10.1175/JCLI-D-14-00477.1.
- Vanhatalo, E., and M. Kulauci, 2016: Impact of Autocorrelation on Principal Components and Their Use in Statistical Process Control. *Qual. Reliab. Engng. Int.*, **32**, 1483–1500, doi:10.1002/qre.1858.
- Ventrice, M. J., M. C. Wheeler, H. H. Hendon, C. J. Schreck, C. D. Thorncroft, and G. N. Kiladis, 2013: A Modified Multivariate Madden–Julian Oscillation Index Using Velocity Potential. *Mon. Wea. Rev.*, **141**, 4197–4210, doi:10.1175/MWR-D-12-00327.1.
- Vitart, F., 2014: Evolution of ECMWF sub-seasonal forecast skill scores. *Q.J.R. Meteorol. Soc.*, **140**, 1889–1899, doi:10.1002/qj.2256.
- Waliser, D., and Coauthors, 2009: MJO Simulation Diagnostics. *J. Climate*, **22**, 3006–3030.

- Wang, B., and H. Rui, 1990: Synoptic climatology of transient tropical intraseasonal convection anomalies: 1975–1985. *Meteorol. Atmos. Phys.*, **44**, 43–61, doi:10.1007/BF01026810.
- Weare, B. C., and J. S. Nasstrom, 1982: Examples of extended empirical orthogonal function analysis. *Mon. Wea. Rev.*, **110**, 481–485.
- Wheeler, M., and G. N. Kiladis, 1999: Convectively coupled equatorial waves: Analysis of clouds and temperature in the wavenumber frequency domain. *J. Atmos. Sci.*, **56**, 374–399.
- Wheeler, M. C., and H. H. Hendon, 2004: An All-Season Real-Time Multivariate MJO Index: Development of an Index for Monitoring and Prediction. *Mon. Wea. Rev.*, **132**, 1917–1932.
- Yanai, M., B. Chen, and W. Tung, 2000: The Madden–Julian Oscillation Observed during the TOGA COARE IOP: Global View. *J. Atmos. Sci.*, **57**, 2374–2396, doi:10.1175/1520-0469(2000)057<2374:TMJOOD>2.0.CO;2.
- Yoneyama, K., C. Zhang, and C. N. Long, 2013: Tracking Pulses of the Madden–Julian Oscillation. *Bull. Amer. Meteor. Soc.*, **94**, 1871–1891, doi:10.1175/BAMS-D-12-00157.1.
- Zhang, C., 2005: The Madden Julian Oscillation. *Rev. Geophys.*, **43**, **RG2003**.
- Zhang, C., 2013: Madden–Julian Oscillation: Bridging Weather and Climate. *Bull. Amer. Meteor. Soc.*, **94**, 1849–1870, doi:10.1175/BAMS-D-12-00026.1.
- , J. Gottschalck, E. D. Maloney, M. W. Moncrieff, F. Vitart, D. E. Waliser, B. Wang, and M. C. Wheeler, 2013: Cracking the MJO nut. *Geophysical Research Letters*, **40**, 1223–1230, doi:10.1002/grl.50244.

## List of Figures:

### **Figs. From sec.4a**

**Fig.1a.** Spectral plots of RMM1 and RMM2 (PC1 and PC2 of Combined EEOF modes), following WH04.

**Fig.1b.** The scatter plot of [RMM1, RMM2] phases. The phase space is demarked into 8 equal divisions.

**Fig.2.** Composite of eight phases in sequential pattern each showing the life cycle of canonical MJO, following WH. Left panel is for OLR anomaly & right panel is for CHI200 anomaly.

**Fig.3.** Hovmoller plot of (a) OLR and (b) Chi200 anomalies obtained from Fig.2 with meridional averaging between 15°S-15°N. It shows eastward propagation.

### **Figs. From sec.4b**

**Fig.4.** Combined EOF modes describing the longitudinal variation of MJO (similar to Fig.1. of WH04) with standardized indices as discussed in sec.4b.

**Fig.5a.** Same as Fig.1a except with standardization of indices as discussed in section 4(b).

**Fig.5b.** Same as Fig.2 except with standardization of indices.

### **Figs. From sec.4c**

**Fig.6a.** Same as Fig.5a except OLR field is replaced with Velocity Potential at 200hpa field as discussed in section 4(c).

**Fig.6b.** Same as Fig.5b except for input OLR field is replaced with Velocity Potential at 200hpa field (Chi200).

### **Figs. From sec.4d**

**Fig.7a.** Same as Fig.6a except with spatial averaging as discussed in section 4(d).

**Fig.7b.** Same as Fig.6b except the computation of the combined EOFs are done with spatial averaged data.

### **Figs. From sec.4e**

**Fig.8a.** Same as Fig.7a except with EEOF technique as discussed in section 4(e).

**Fig.8b.** Same as fig.7b except the computation of the EOF with extended data matrix, i.e. EEOF as discussed in section 4(e).

**Fig.9.**Hovmuller plot of (a) OLR and (b) CHI200 anomalies based on EEOF technique.

#### **Figs. From sec.4f**

**Fig.10.** Spatial composite for 15<sup>th</sup> Jan of (a) OLR, (c) Chi200, (e) precipitation and for 15<sup>th</sup> July (b) OLR, (d) chi200 (f) precipitation anomalies.

**Fig.11.**Hovmoller plots for OLR anomalies (in  $W/m^2$ ; shaded) & U850 anomalies (contour, positive solid & negative dashed, contour interval 1 m/s) to show Eastward propagation: (a) 15<sup>th</sup> Jan (b) 15<sup>th</sup> Feb (c) 15<sup>th</sup> Mar (d) 15<sup>th</sup> April (e) 15<sup>th</sup> May (f) 15<sup>th</sup> June (g) 15<sup>th</sup> July (h) 15<sup>th</sup> Aug (i) 15<sup>th</sup> Sep (j) 15<sup>th</sup> Oct (k) 15<sup>th</sup> Nov (l) 15<sup>th</sup> Dec.

**Fig.12.**Hovmoller plots for OLR anomalies (shaded) & relative vorticity anomalies at 850hPa (contour, positive solid & negative dashed, contour interval  $1 \times 10^{-6} s^{-1}$ ) to show northward propagation: (a) 15<sup>th</sup> Jan (b) 15<sup>th</sup> Feb (c) 15<sup>th</sup> Mar (d) 15<sup>th</sup> April (e) 15<sup>th</sup> May (f) 15<sup>th</sup> June (g) 15<sup>th</sup> July (h) 15<sup>th</sup> Aug (i) 15<sup>th</sup> Sep (j) 15<sup>th</sup> Oct (k) 15<sup>th</sup> Nov (l) 15<sup>th</sup> Dec.

**Fig.13.** Hovmoller plots for precipitation anomalies to show Eastward propagation: (a) 15<sup>th</sup> Jan (b) 15<sup>th</sup> Feb (c) 15<sup>th</sup> Mar (d) 15<sup>th</sup> April (e) 15<sup>th</sup> May (f) 15<sup>th</sup> June (g) 15<sup>th</sup> July (h) 15<sup>th</sup> Aug (i) 15<sup>th</sup> Sep (j) 15<sup>th</sup> Oct (k) 15<sup>th</sup> Nov (l) 15<sup>th</sup> Dec.

**Fig.14.** Hovmoller plots for precipitation anomalies to show northward propagation: (a) 15<sup>th</sup> Jan (b) 15<sup>th</sup> Feb (c) 15<sup>th</sup> Mar (d) 15<sup>th</sup> April (e) 15<sup>th</sup> May (f) 15<sup>th</sup> June (g) 15<sup>th</sup> July (h) 15<sup>th</sup> Aug (i) 15<sup>th</sup> Sep (j) 15<sup>th</sup> Oct (k) 15<sup>th</sup> Nov (l) 15<sup>th</sup> Dec.

#### **Figs. From sec.4g**

**Fig.15.** Reconstructed OLR anomalies over Central India and Indian Ocean. Black curve is based on lagged phase composite method (-45 day to +45 day, as discussed in Sec.4f) and red curve is based on simple phase composite method (considering all the days of the year).

#### **Figures from Sec.5a**

**Fig.16.** (PC1, PC2) phase space plot during 2009 SOND (a) Conventional WH method, (b) same as 16(a) except Standardization of indices, (c) Same as 16(b) except Replacing OLR with Chi200, (d) same as 16(c) except Spatial averaging, (e) same as 16(d) except with EEOF technique.

#### **Figures from Sec.5b**

**Fig.17a.** Hovmoller plot of Unfiltered OLR anomaly (shaded), superimposed over it (contours) is the 20-90 day Lanczos filtered OLR anomaly during the DYNAMO period.

**Fig.17b.** Hovmoller plot of MJO filtered OLR (shaded), superimposed over it (contours) is the 20-90 day Lanczos filtered OLR anomalies during the DYNAMO period.

**Fig.18.** Comparison of MJO1 and MJO2 tracking during DYNAMO period based on (a) WH04 method (b) EEOF method.

### Figures from Sec.5c

**Fig.19.** 2015 monsoon tracking based on (a) WH method and (b) EEOF method.

### Figures from Sec.5d

**FIG.20.** The two TOGA COARE MJO events between 28 Nov 1992 and 15 Feb 1993 represented by the RMM and RMM\_L for (a) raw OLR anomaly (shading) and filtered MJO (contour with interval  $5 \text{ W/m}^2$  and 0 being omitted); (b) reconstructed anomalies (shaded) by RMM\_L and total filtered MJO [contour as in (a)]. (c) amplitudes of RMM (Red) and RMM-L (blue);. Wavnumber-Frequency filter in the range of wavenumber 1-5 and 20-100 day are used based on 2-D spectral decomposition as suggested by Wheeler and Kiladis (1999). (d) similar to fig 20(b) except with regression based reconstruction.

**FIG. 21.** Cartesian phase diagrams of RMM\_L for the two events during TOGA COARE (a) 28 Nov 1992–5 Jan 1993 and (b) 1 Jan–15 Feb 1993.

**FIG.22.** (a) and (b) are same as Fig.20 (a) and (b) respectively, but for the velocity potential at 200hpa ( $\chi_{200}$ ). (C) Same as Fig.20 (d) (i.e. based on regression based reconstruction) but for  $\chi_{200}$ . Contour with interval  $1 \times 10^5 \text{ m}^2/\text{s}$  and 0 being omitted, shaded regions are shown in  $10^5 \text{ m}^2/\text{s}$  units.

### Figures from Sec.5e

**Fig.23.** Season wise statistical skill of model during 2001-2010 CFSv2 Extended range hindcast period.

**Fig.24.** (PC1, PC2) phase space plot for next 25 days for MAY 2016 MJO event. Blue is for Observation and green is for the IITM extended range forecast. (a-e) are for different ICs (as mentioned in the title section of each fig.), (f) phase space plot of RMM index (obtained from Bureau of Meteorology) for MAY 2016.

**Fig.25:** (a)-(b) Shows the space-time power spectra for the symmetric and the anti-symmetric part of actual OLR data (NOAA) averaged between  $15^\circ\text{S}$ - $15^\circ\text{N}$ . (c)-(d) shows the same but using the regression based OLR reconstruction (cf. Sec.4g). Power spectrum has the background removed as discussed in Wheeler and Kiladis (1999).

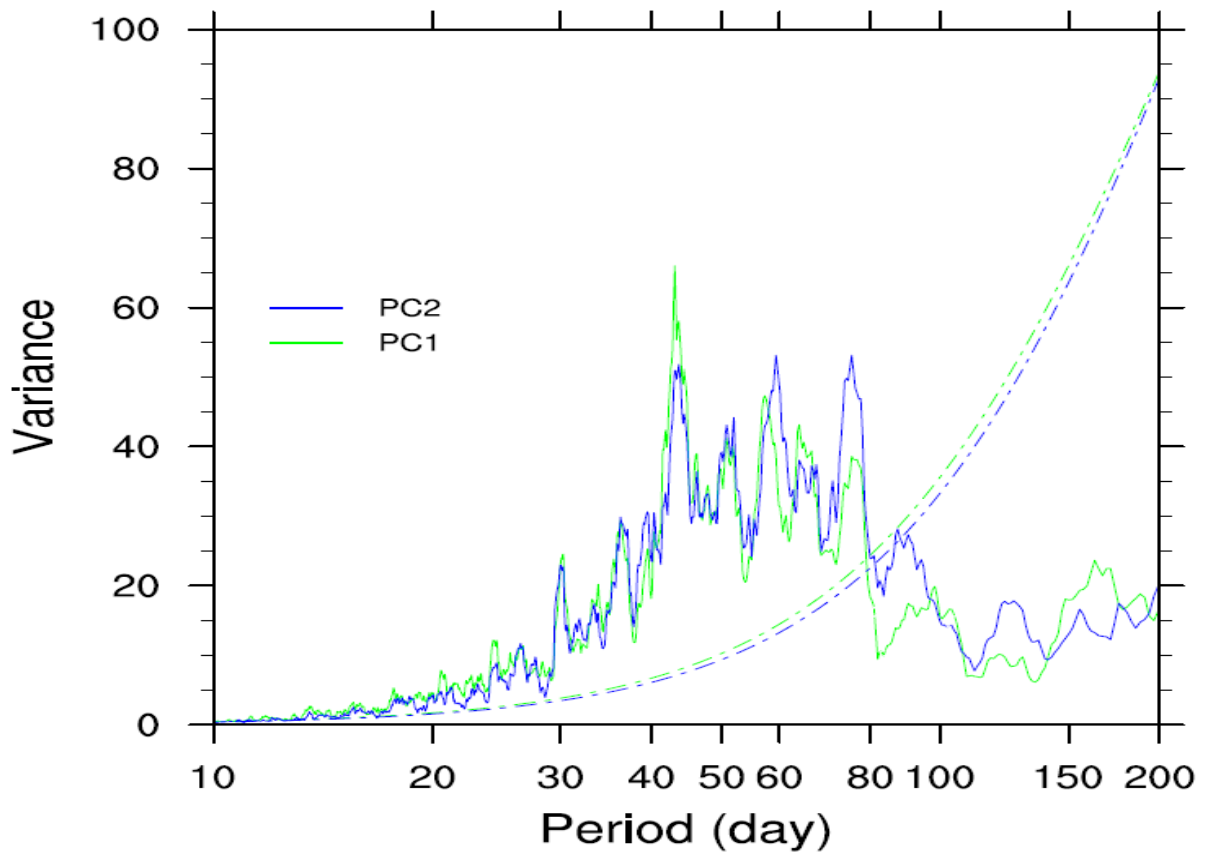


**Fig.1a.** Spectral plots of RMM1 and RMM2 (PC1 and PC2 of Combined EOF modes), Following WH04.

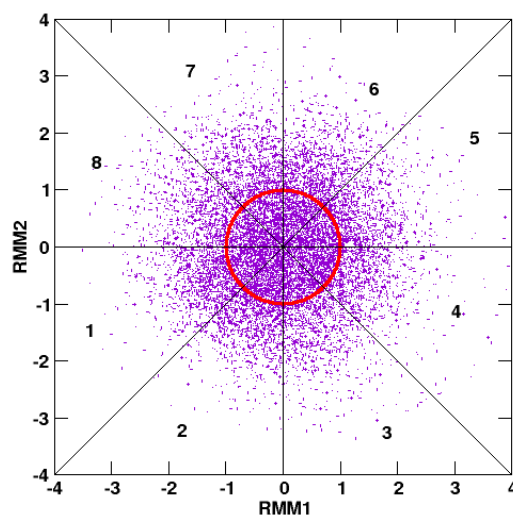


**Fig.1b.** The scatter plot of [RMM1, RMM2] phases. The phase space is demarcated into 8 equal divisions.

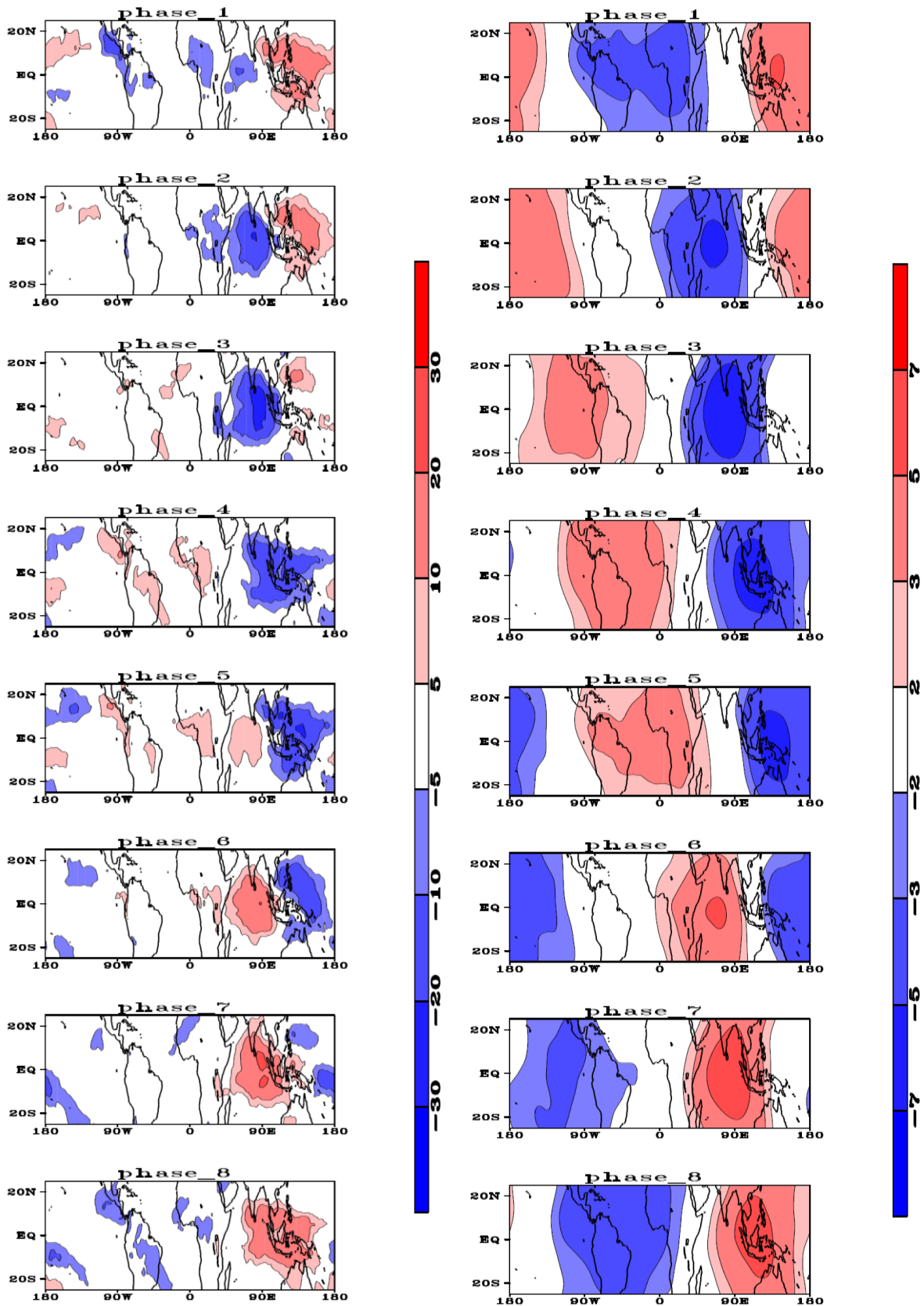


**Fig.2.** Composite of eight phases in sequential pattern each showing the life cycle of canonical MJO, following WH. Left panel is for OLR anomaly ( $\text{W/m}^2$ ) & right panel is for CHI200 anomaly ( $1 \times 10^6 \text{ m}^2/\text{s}$ ). Negative **chi200** anomalies represent upper-level divergence.

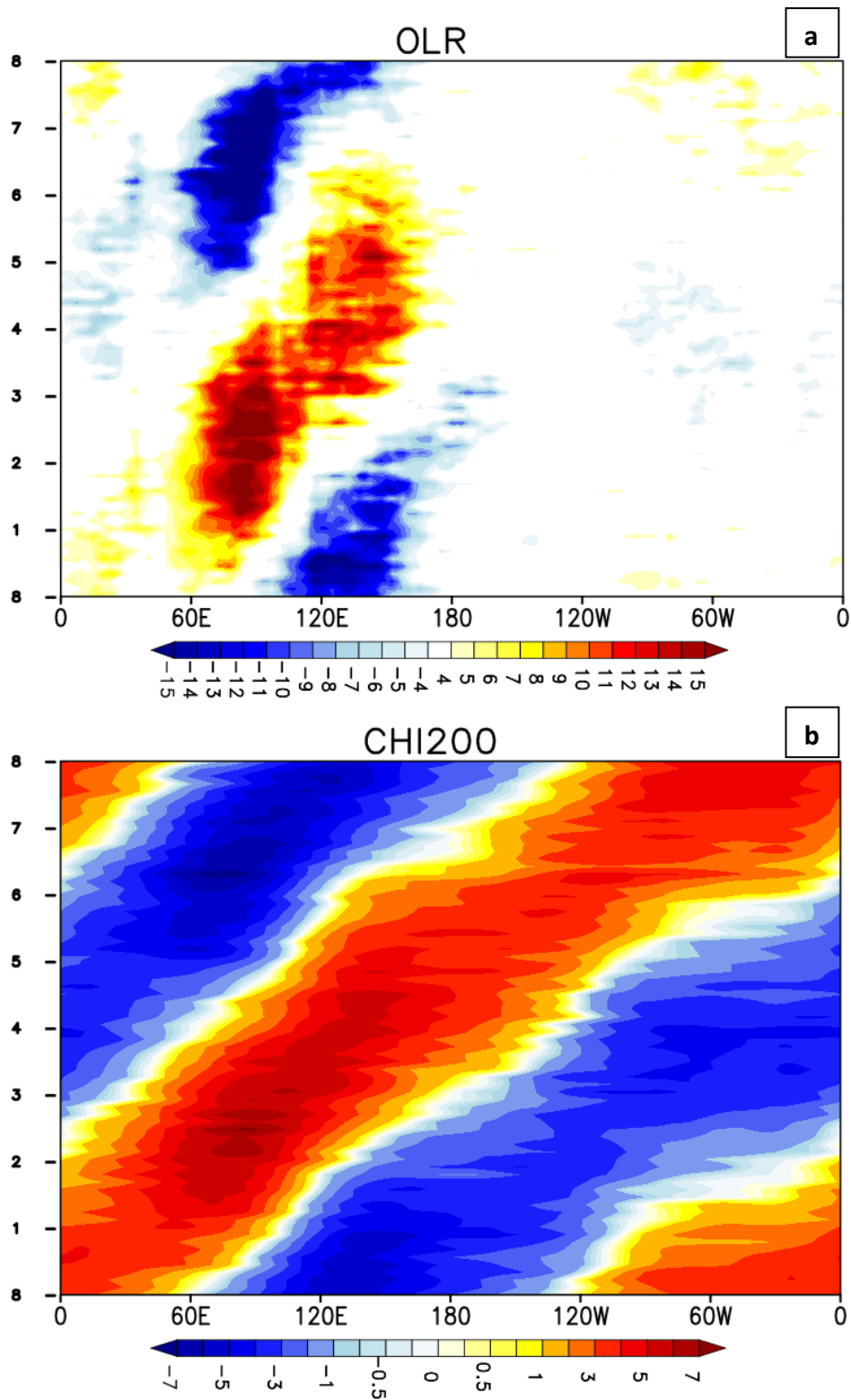


**Fig.3.** Hovmoller plot of (a) OLR anomalies ( $W/m^2$ ) and (b) Chi200 anomalies ( $1 \times 10^6 m^2/s$ ) obtained from Fig.2 with meridional averaging between  $15^\circ S$ - $15^\circ N$ . It shows eastward propagation.

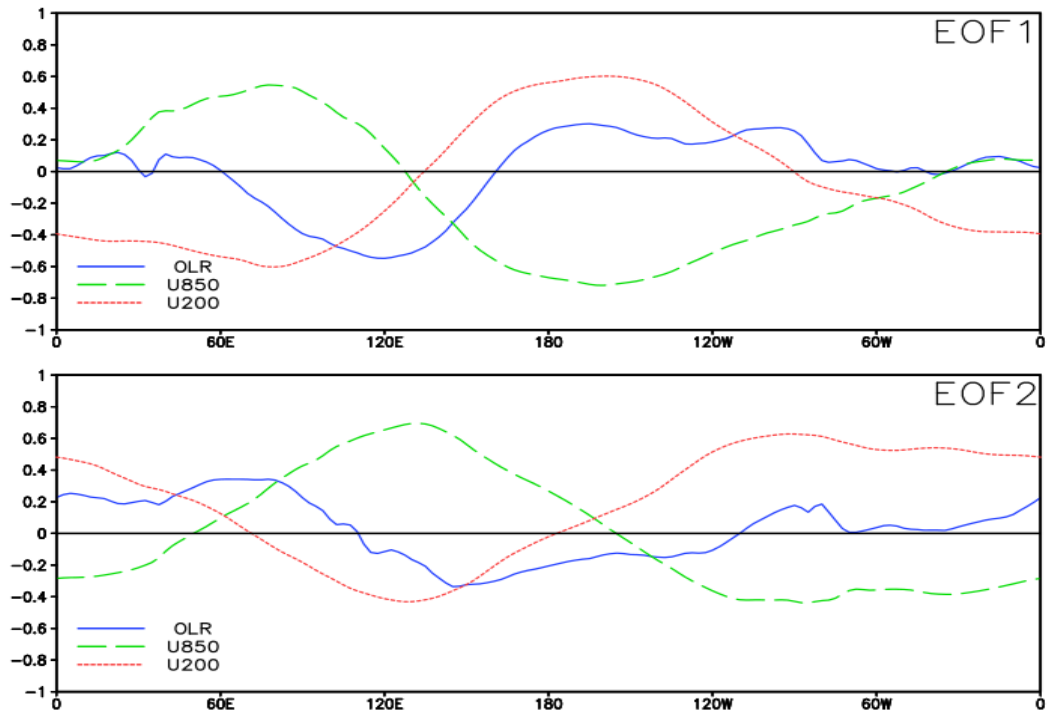


**Fig.4.** Combined EOF modes describing the longitudinal variation of MJO (similar to Fig.1. of WH04) with standardization of indices as discussed in sec.4b.

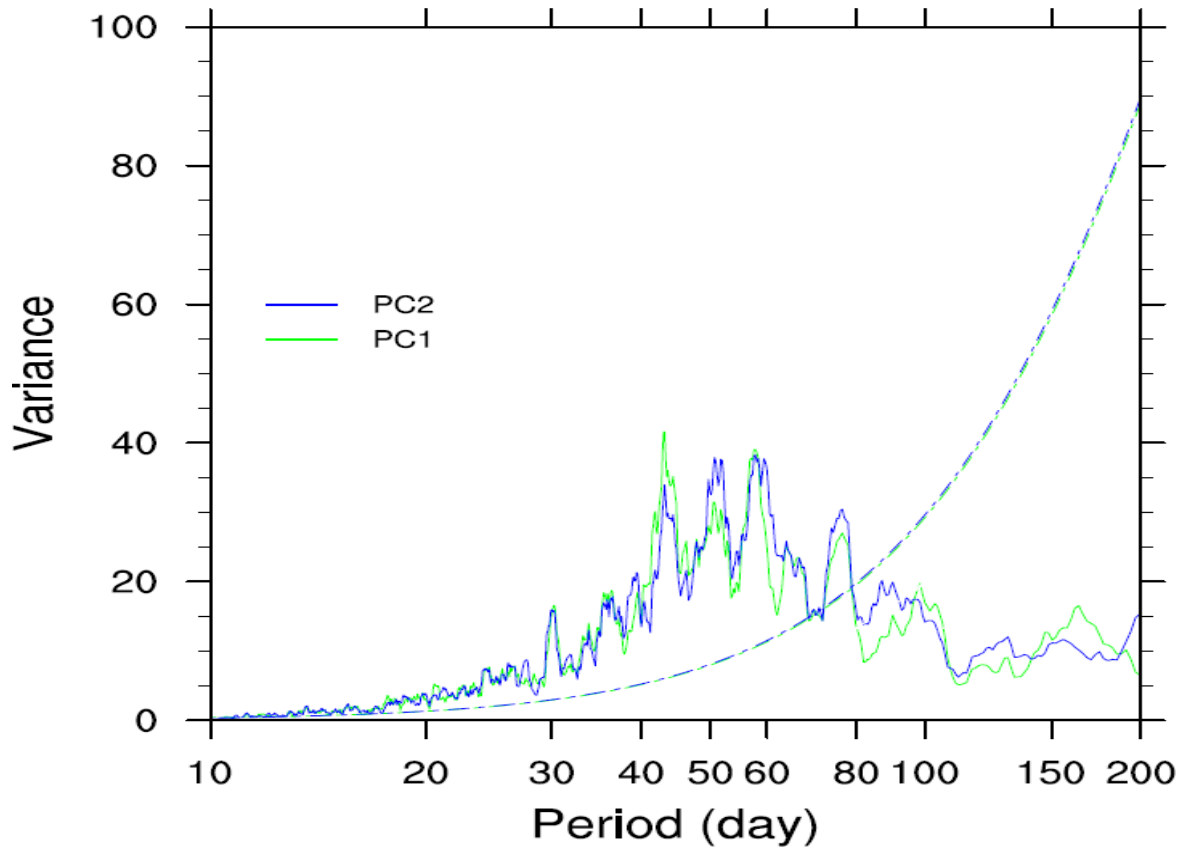


**Fig.5a.** Same as Fig.1a except with standardized indices as discussed in section 4(b).

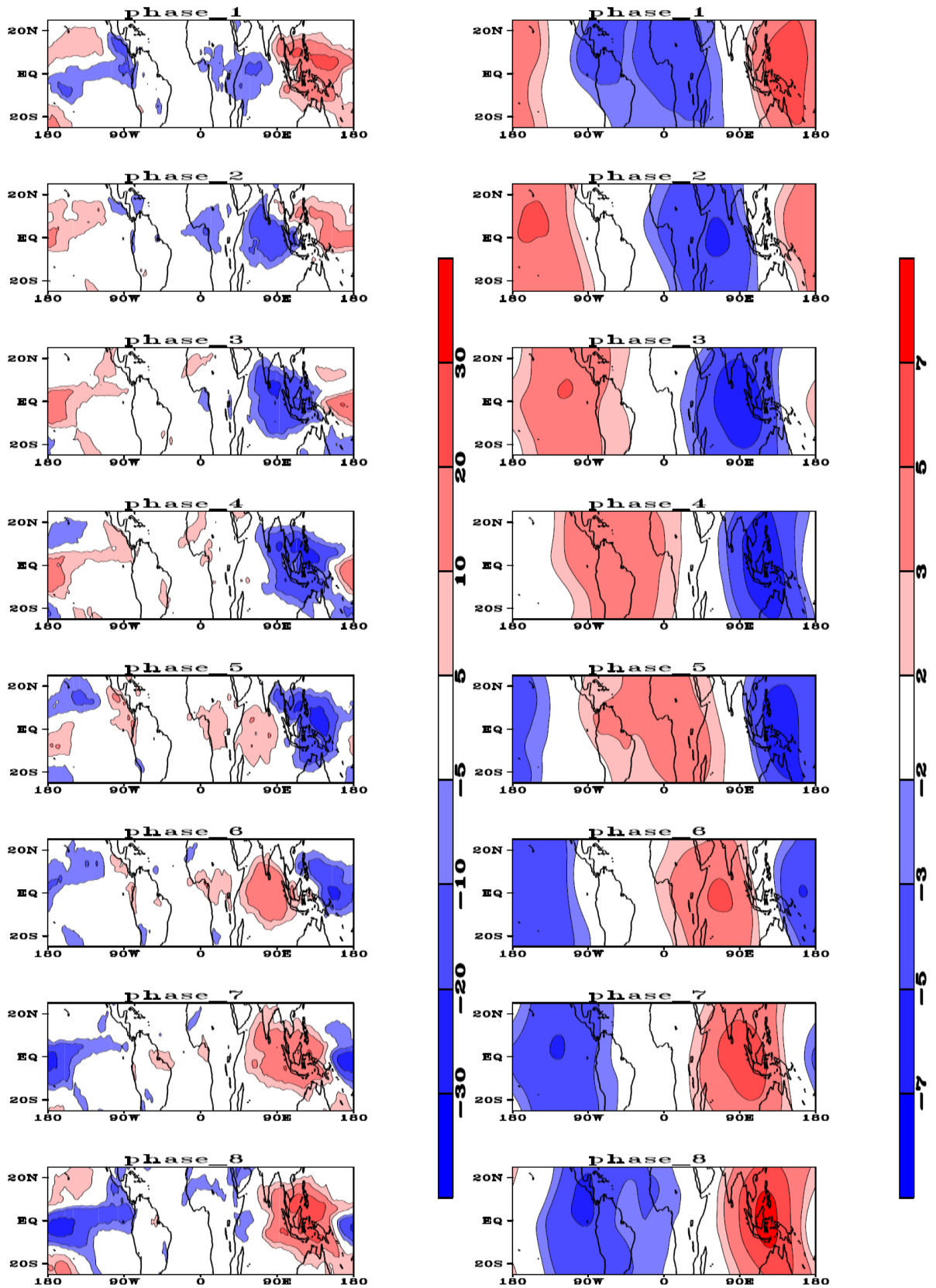
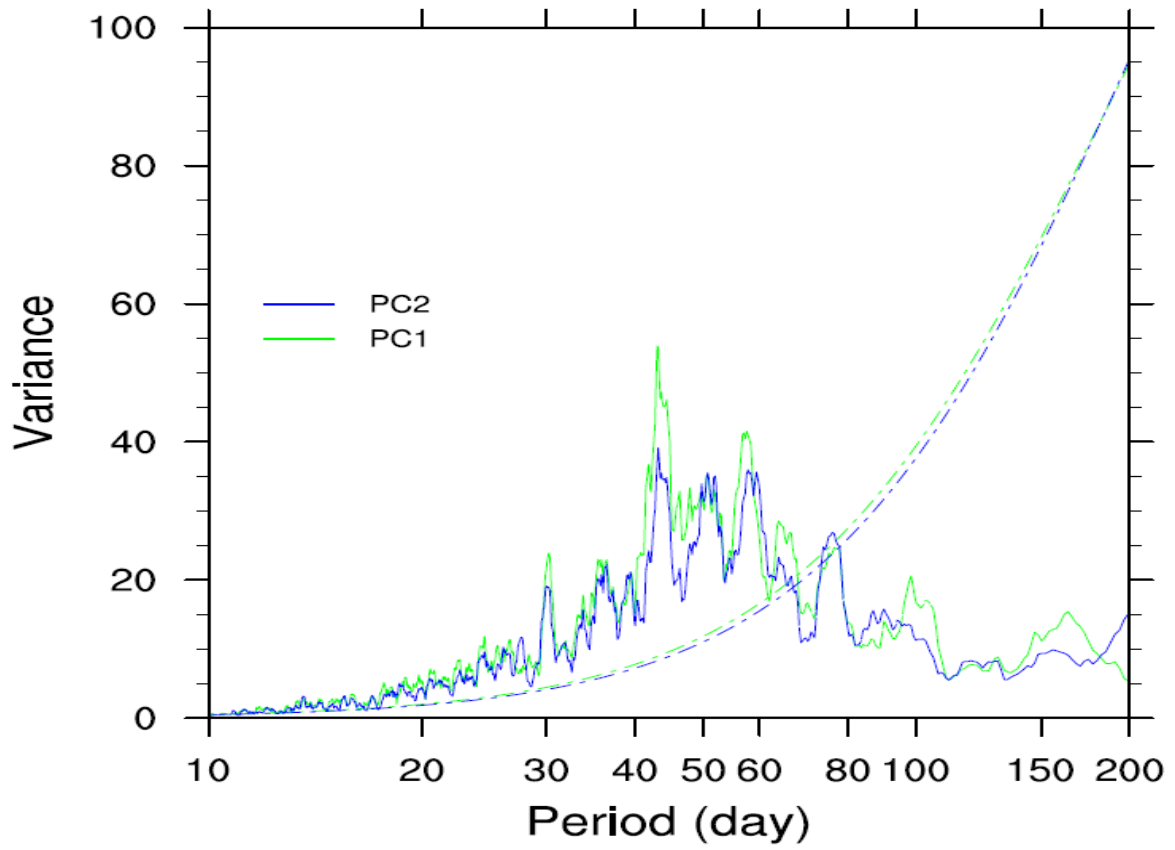
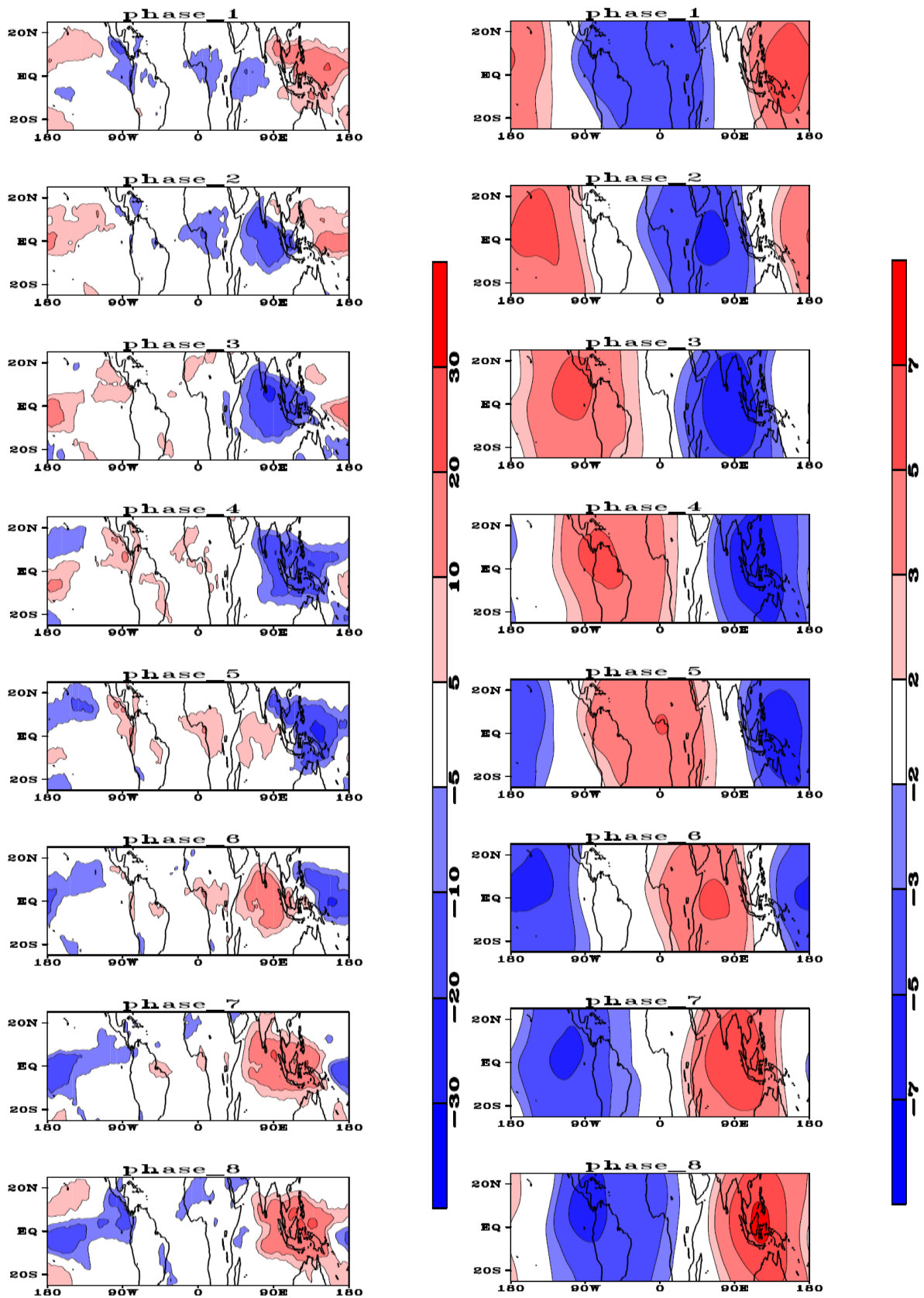


Fig.5b. Same as Fig.2 except with standardization of indices.



**Fig.6a.** Same as Fig.5a except OLR field is replaced with Velocity Potential at 200hpa field as discussed in section 4(c).



**Fig.6b.** Same as Fig.5b except for input OLR field is replaced with Velocity Potential at 200hpa field (Chi200).

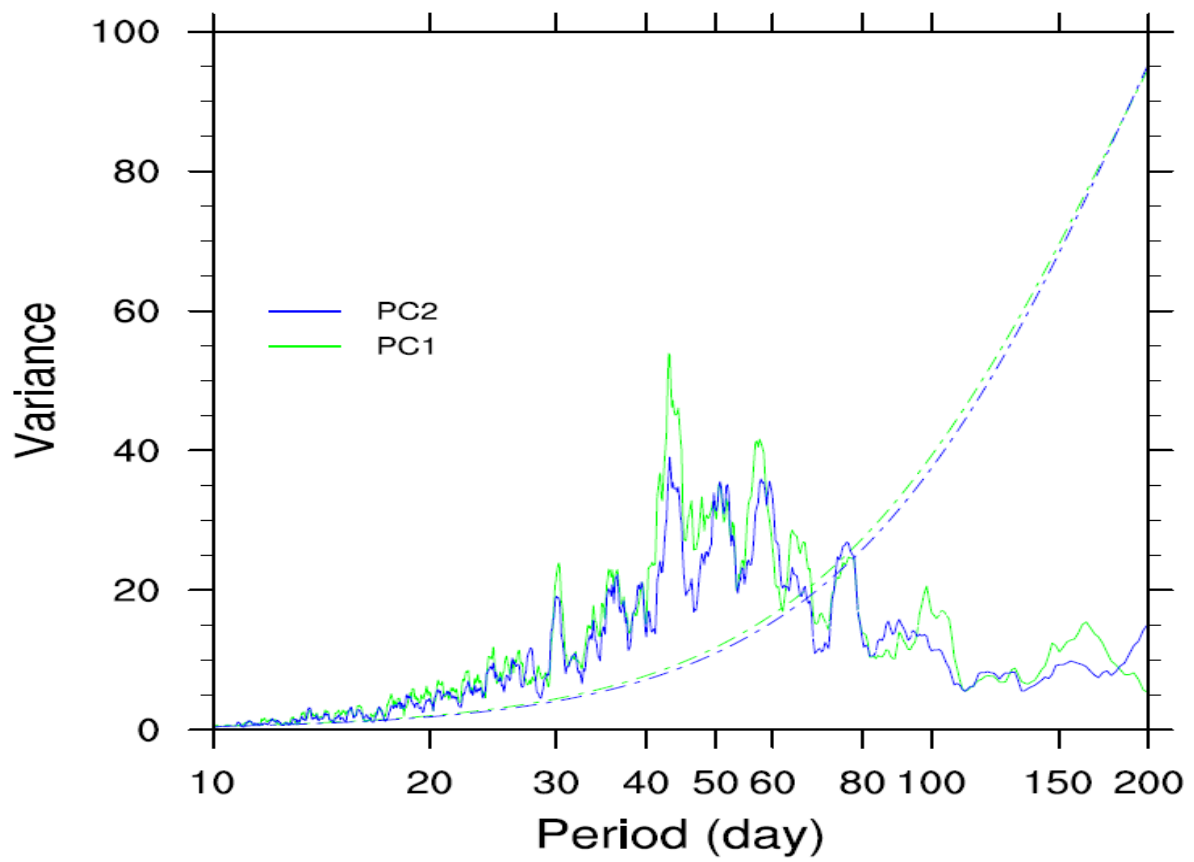


**Fig.7a.** Same as Fig.6a except with spatial averaging as discussed in section 4(d).

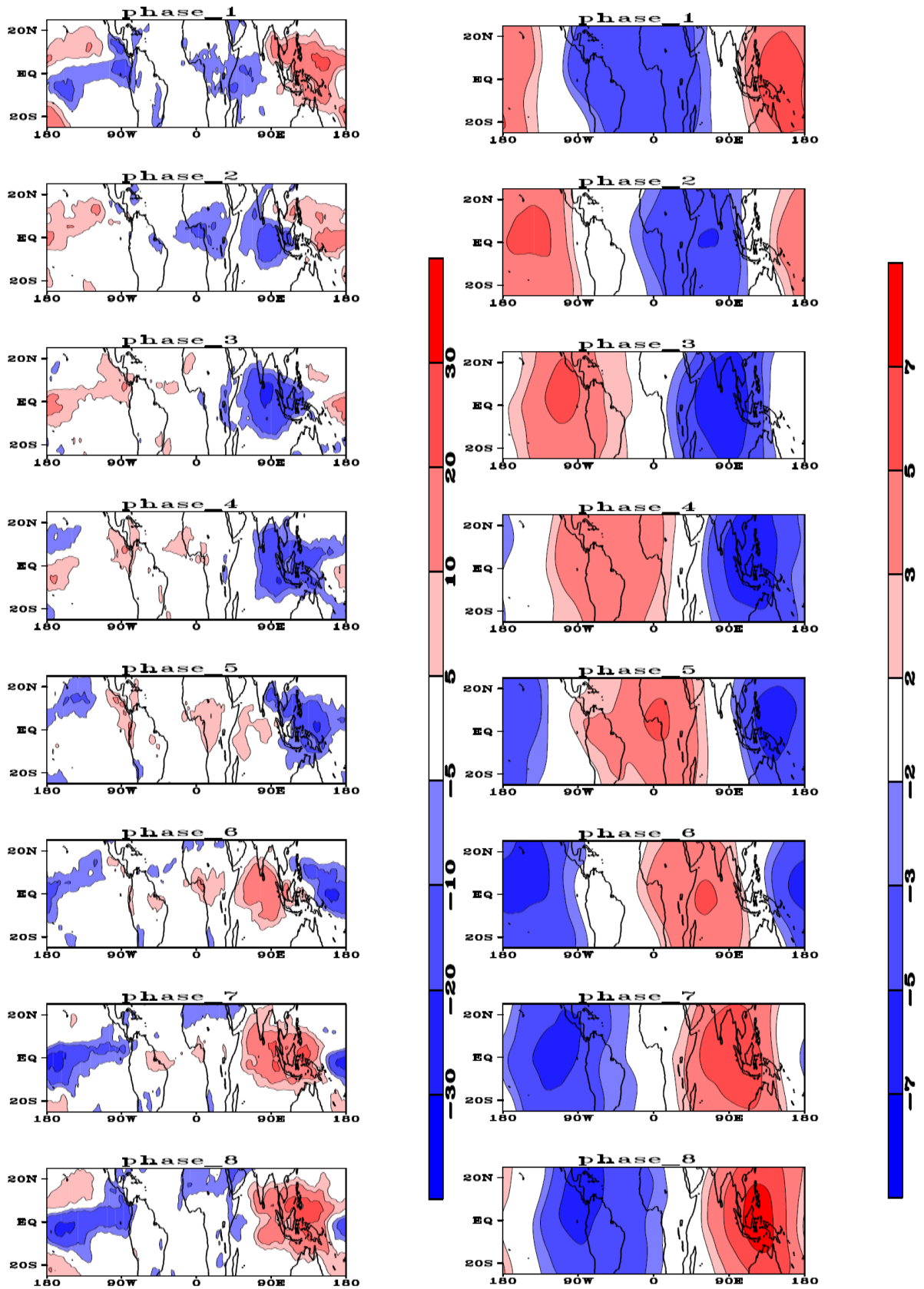


**Fig.7b.** Same as Fig.6b except the computation of the combined EOFs are done with spatial averaged data.

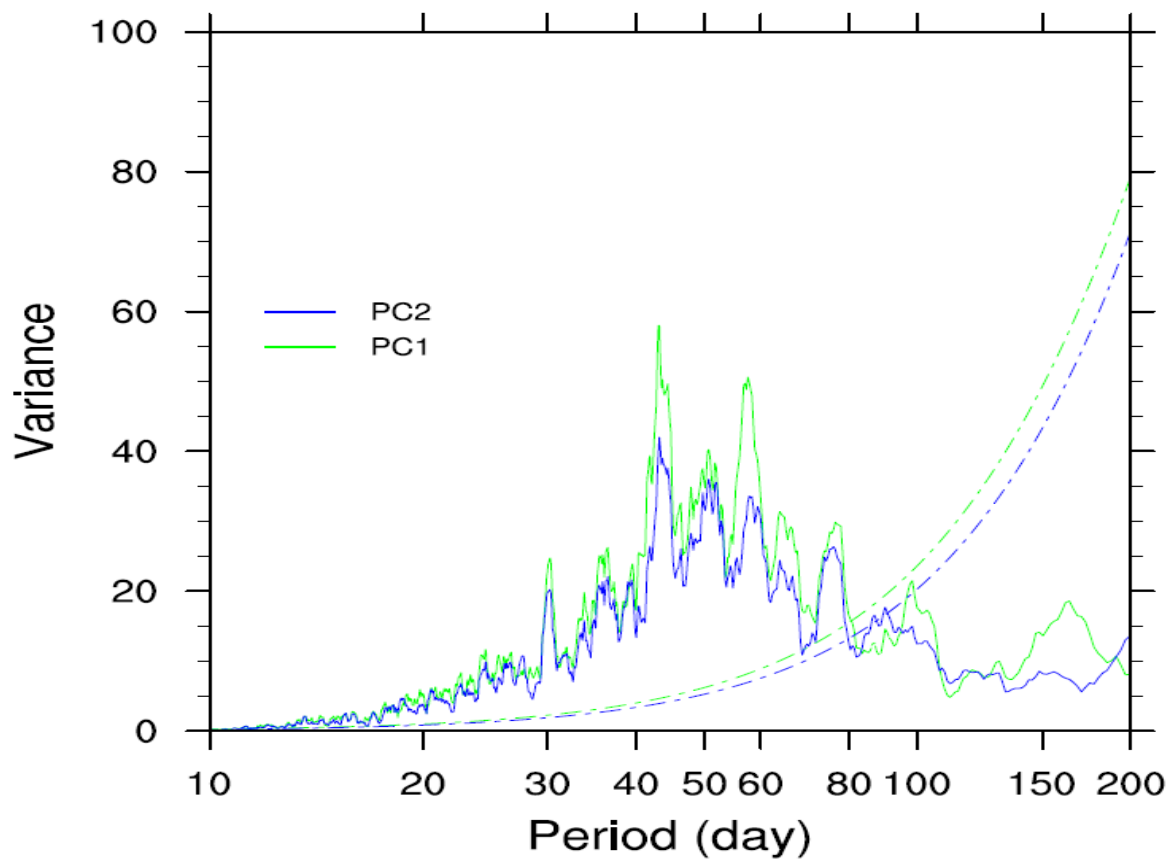


**Fig.8a.** Same as Fig.7a except with EEOF technique as discussed in section 4(e).

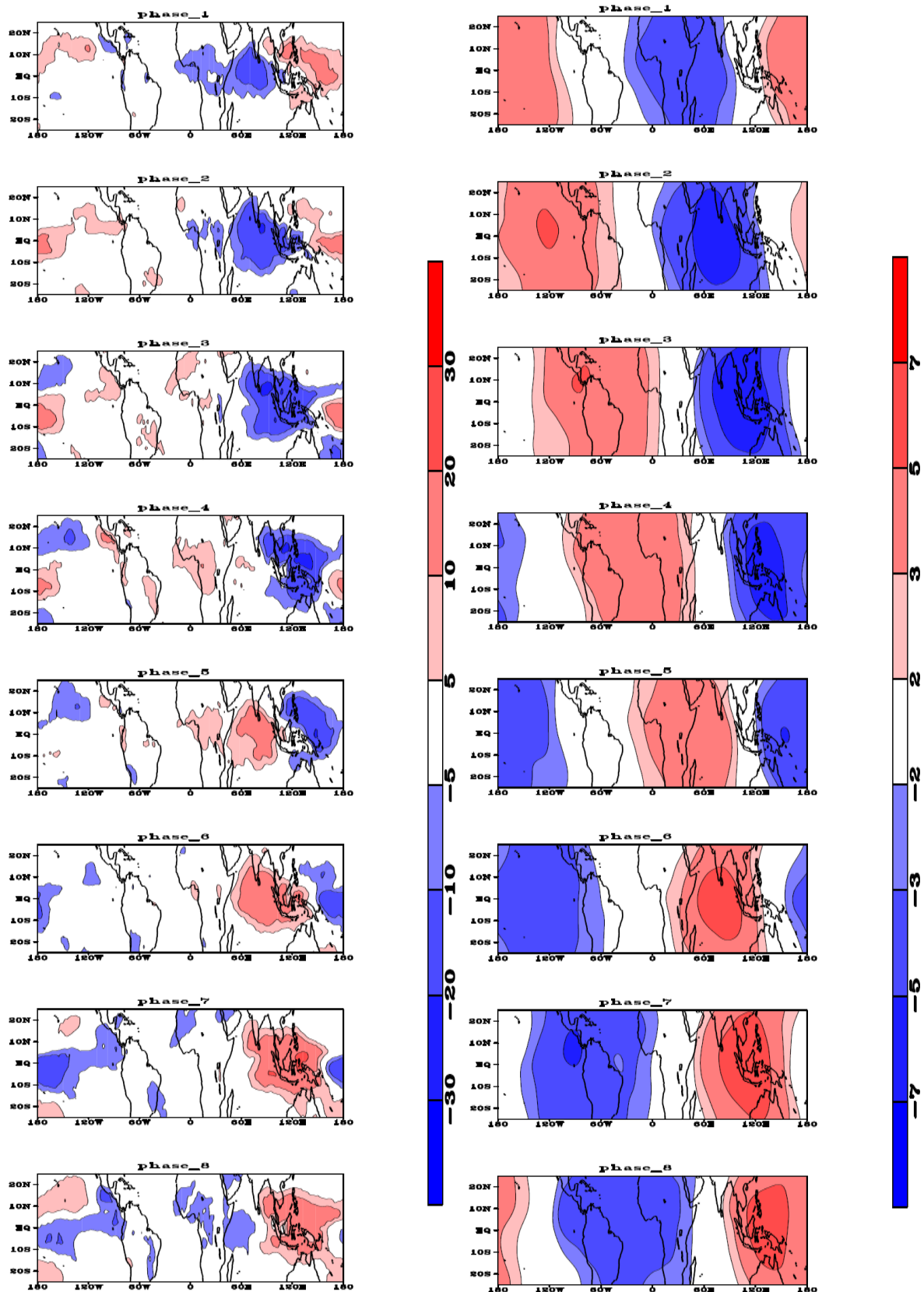


**Fig.8b.** Same as fig.7b except the computation of the EOF with extended data matrix, i.e. EEOF as discussed in section 4(e).

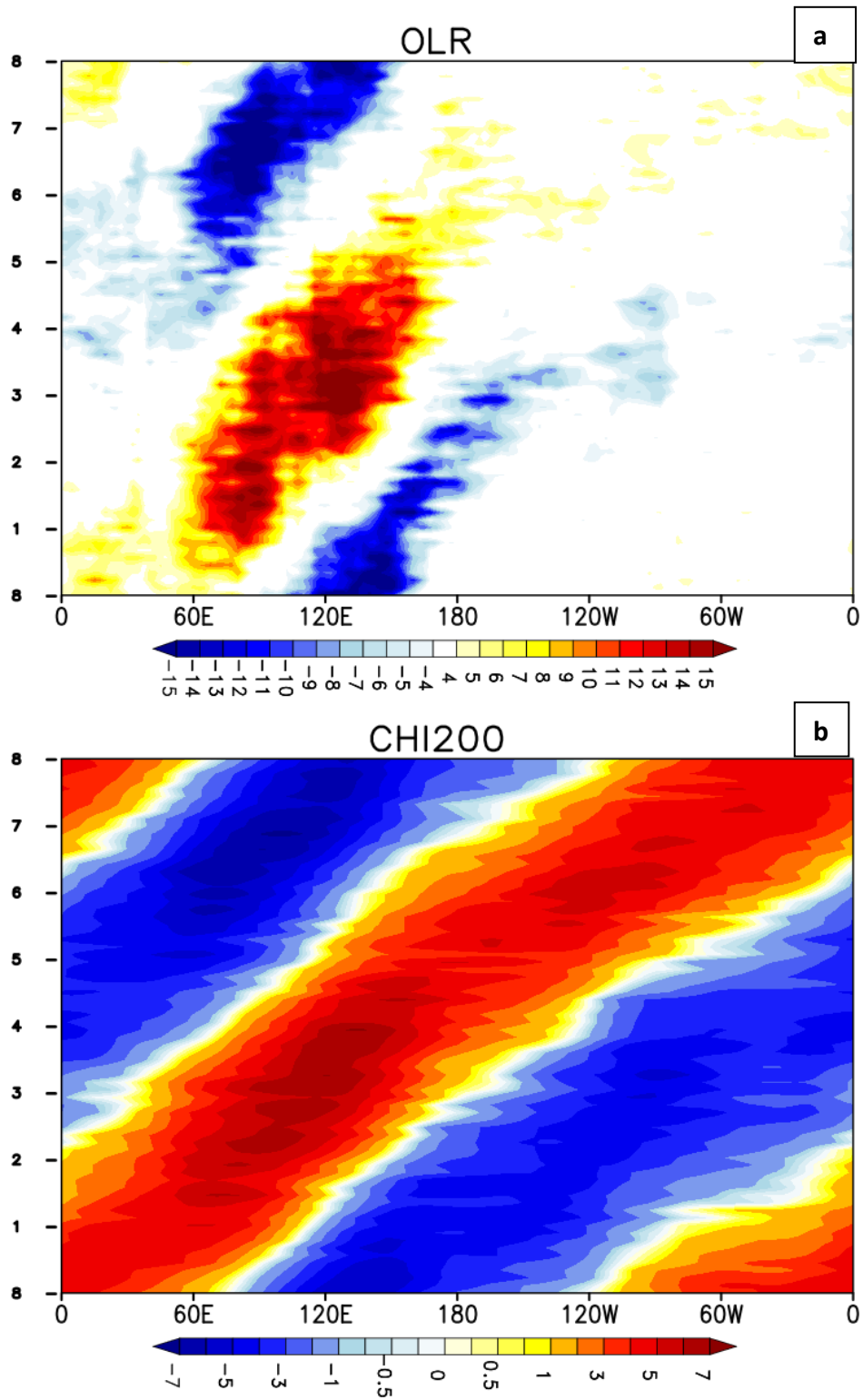


**Fig.9.**Hovmuller plot of (a) OLR anomalies ( $W/m^2$ ) and (b) CHI200 anomalies ( $1 \times 10^6 m^2/s$ ) based on EEOF technique.

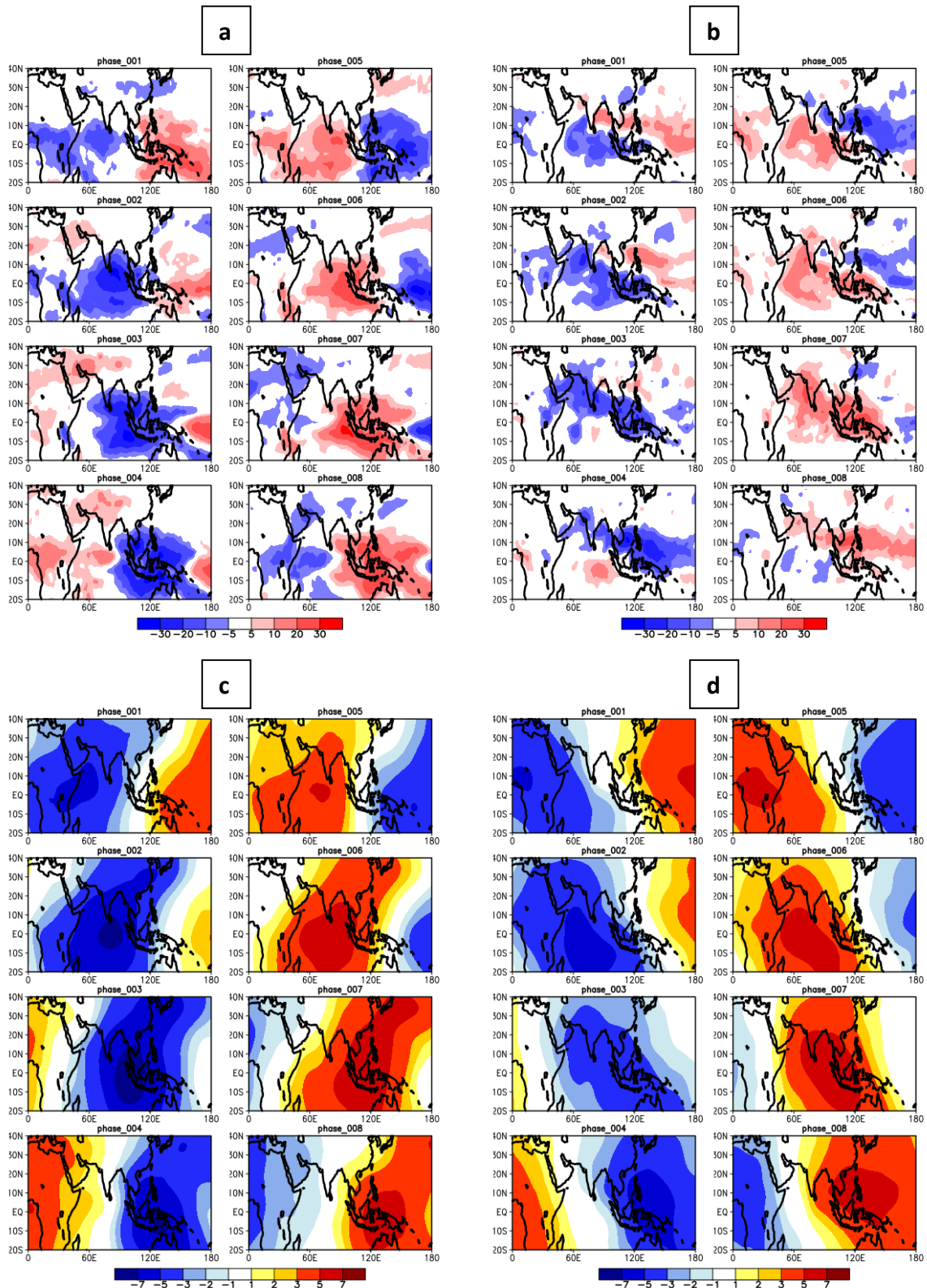


**Fig.10.** Spatial composite of OLR anomaly ( $\text{W/m}^2$ ) for (a) 15<sup>th</sup> Jan (b) 15<sup>th</sup> July and for chi200 anomaly ( $1 \times 10^6 \text{ m}^2/\text{s}$ ) (c) 15<sup>th</sup> Jan (d) 15<sup>th</sup> July.

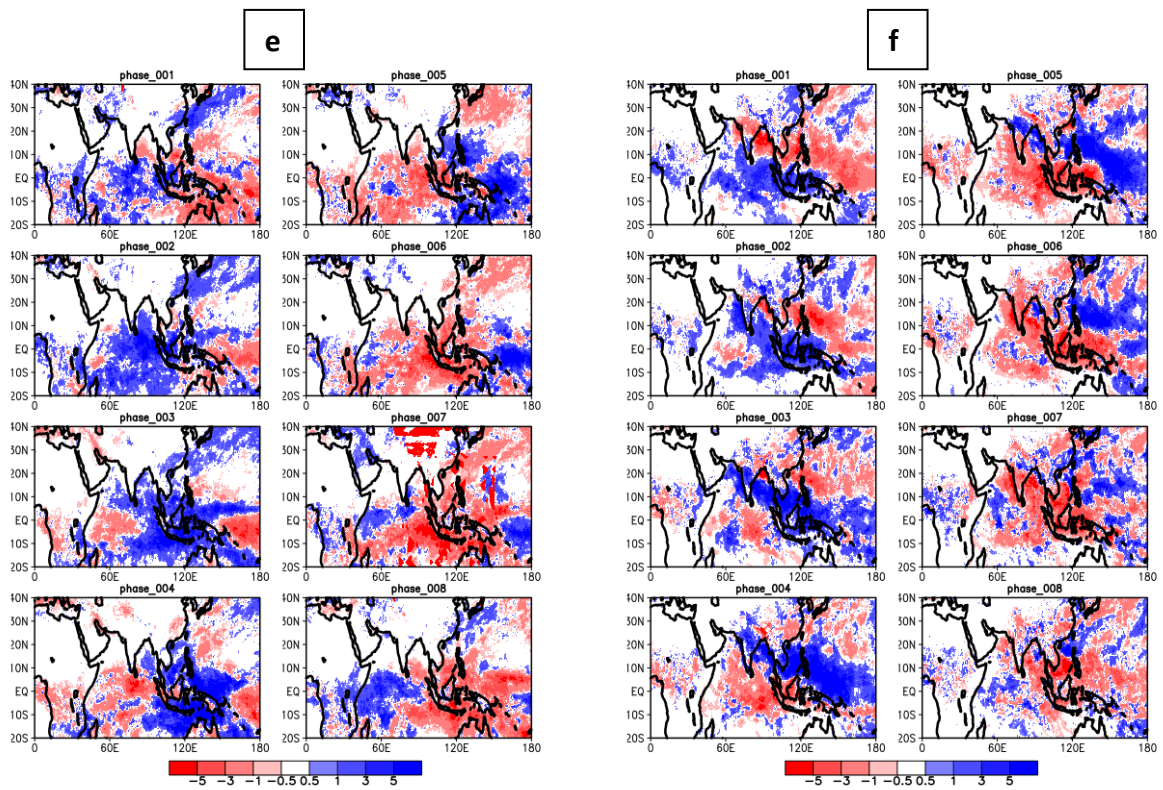


**Fig.10.** (continued) for precipitation anomaly (mm/day) (e) 15<sup>th</sup> Jan (f)15<sup>th</sup> July

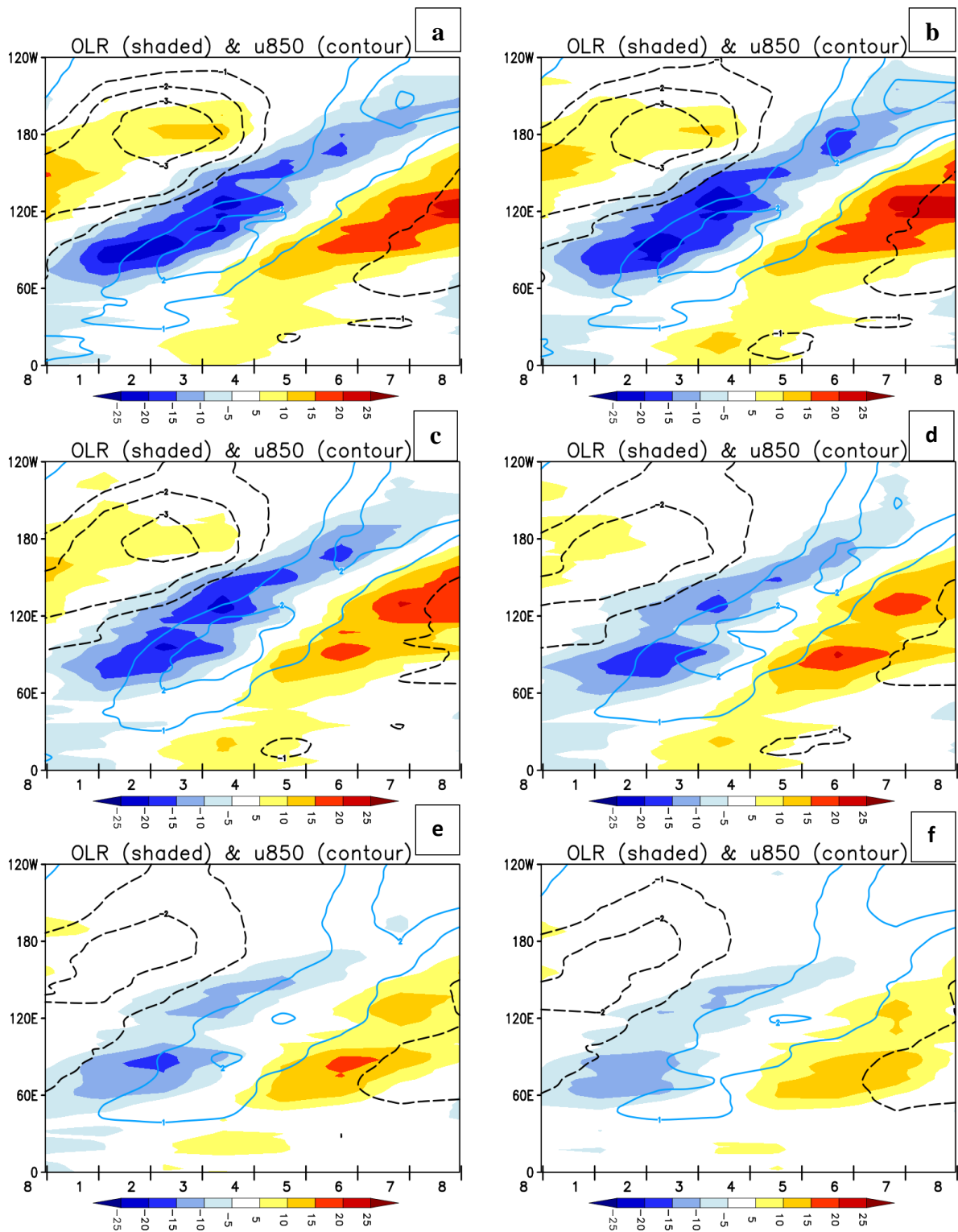


**Fig.11.**Hovmoller plots for OLR anomalies (in  $W/m^2$ ; shaded) & U850 anomalies (contour, positive solid & negative dashed, contour interval 1 m/s) to show Eastward propagation: (a) 15<sup>th</sup> Jan (b) 15<sup>th</sup> Feb (c) 15<sup>th</sup> Mar (d) 15<sup>th</sup> April (e) 15<sup>th</sup> May (f) 15<sup>th</sup> June.

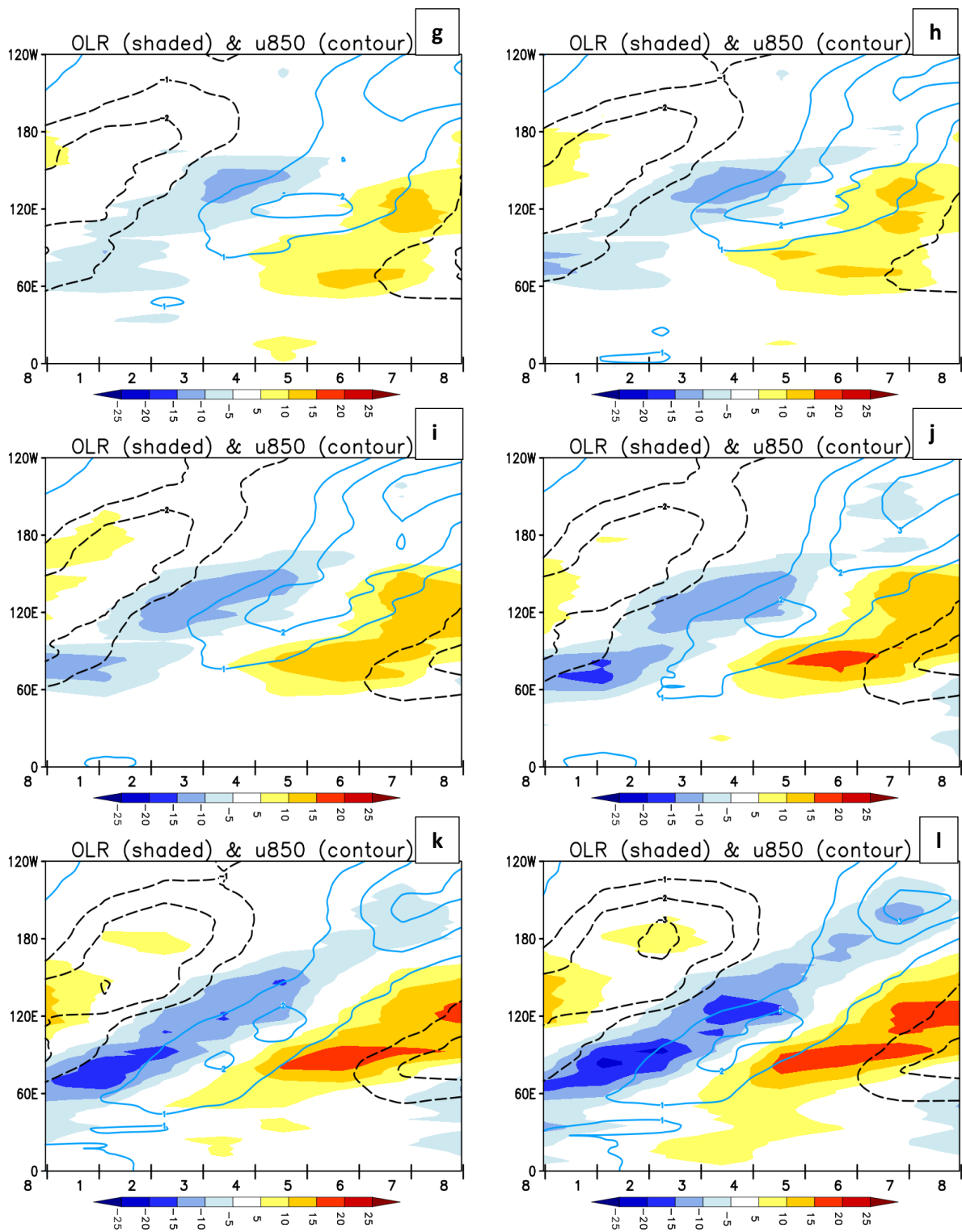


**Fig.11.** (continued) (g) 15<sup>th</sup> July (h) 15<sup>th</sup> Aug (i) 15<sup>th</sup> Sep (j) 15<sup>th</sup> Oct (k) 15<sup>th</sup> Nov (l) 15<sup>th</sup> Dec

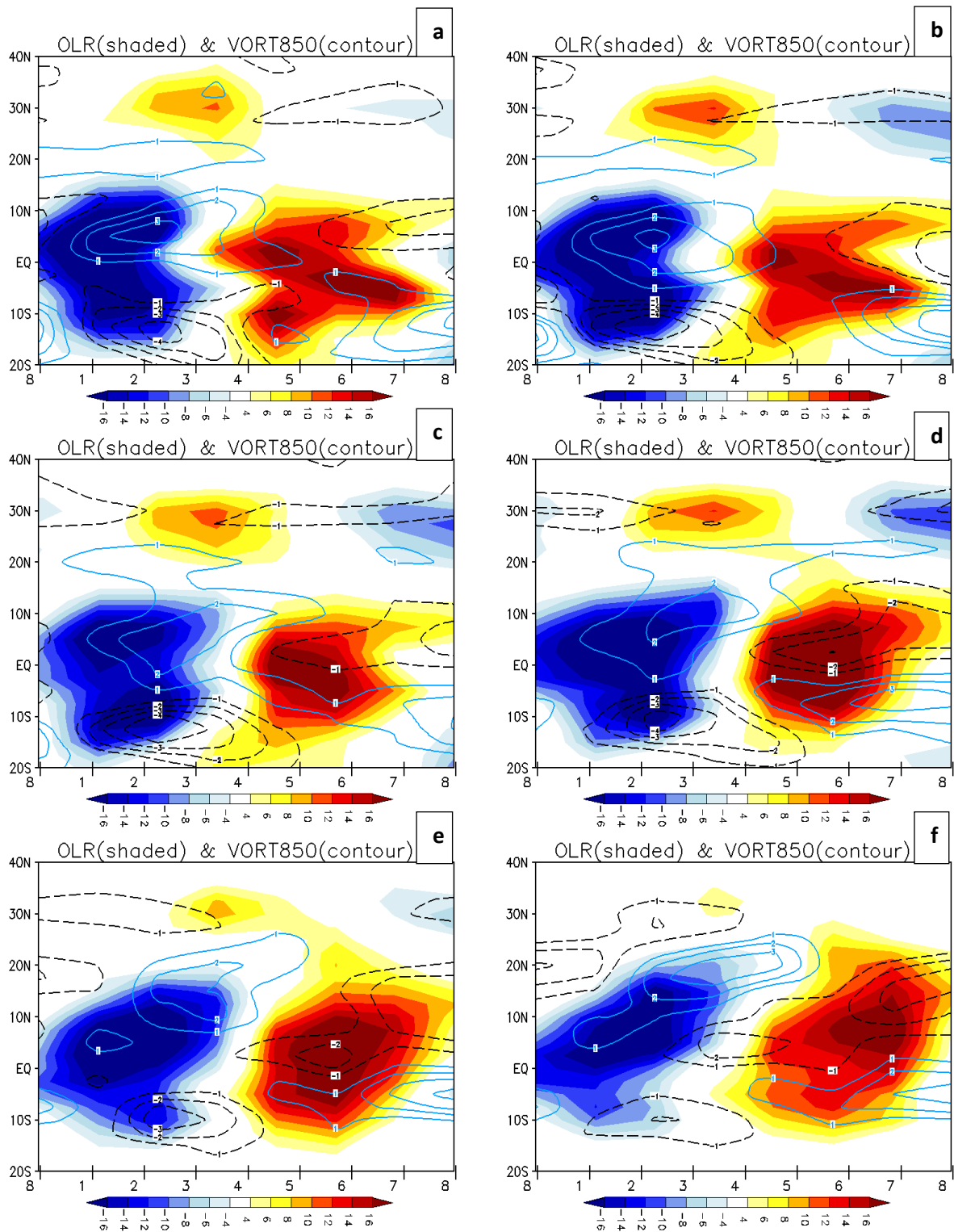


**Fig.12.** Hovmöller plots for OLR anomalies (shaded) & relative vorticity anomalies at 850hPa (contour, positive solid & negative dashed, contour interval  $1 \times 10^{-6} \text{ s}^{-1}$ ) to show northward propagation: (a) 15<sup>th</sup> Jan (b) 15<sup>th</sup> Feb (c) 15<sup>th</sup> Mar (d) 15<sup>th</sup> April (e) 15<sup>th</sup> May (f) 15<sup>th</sup> June

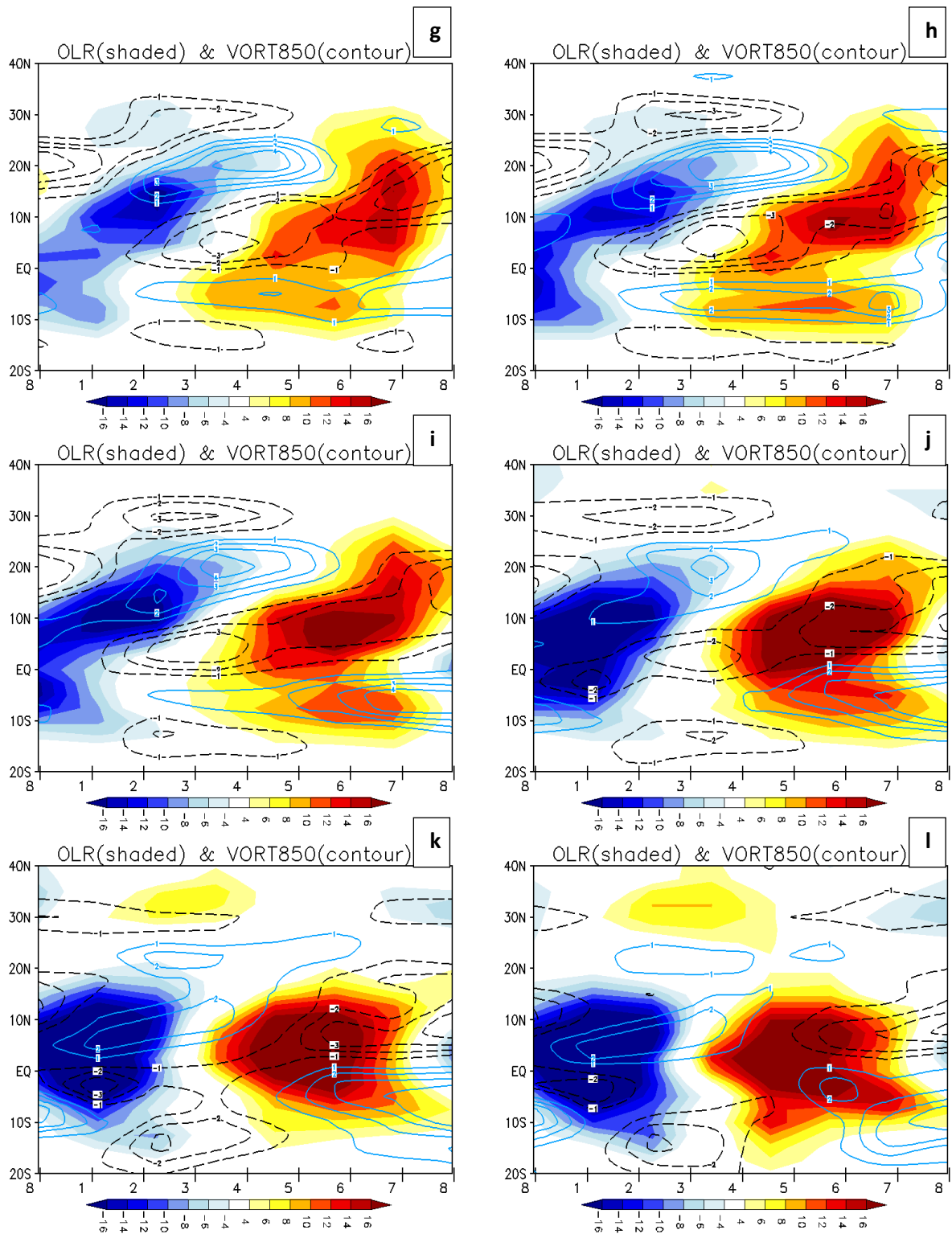


**Fig.12.** (continued) (g) 15<sup>th</sup> July (h) 15<sup>th</sup> Aug (i) 15<sup>th</sup> Sep (j) 15<sup>th</sup> Oct (k) 15<sup>th</sup> Nov (l) 15<sup>th</sup> Dec

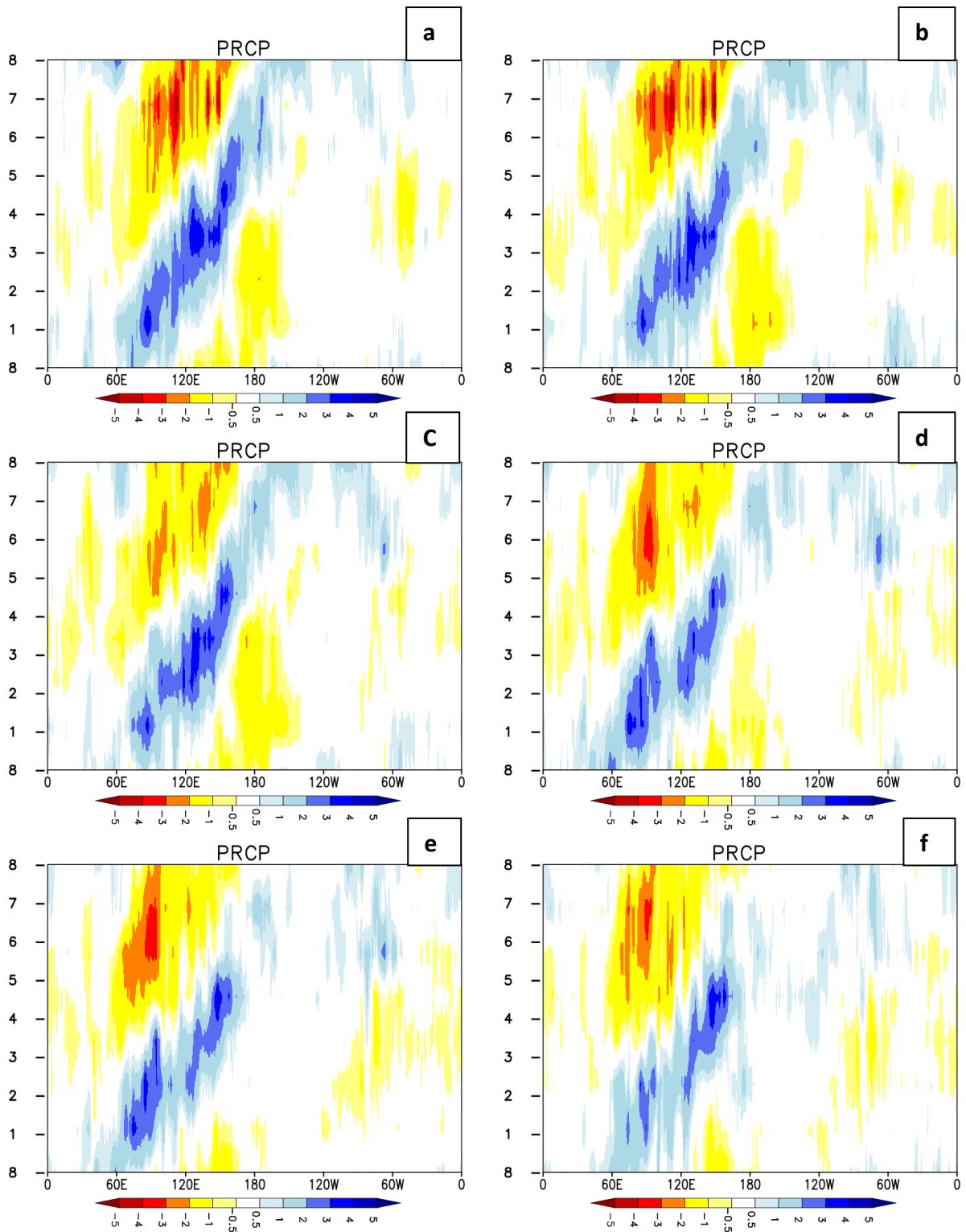


**Fig.13.**Hovmoller plots for precipitation anomalies (mm/day) to show eastward propagation: (a) 15<sup>th</sup> Jan (b) 15<sup>th</sup> Feb (c) 15<sup>th</sup> Mar (d) 15<sup>th</sup> April (e) 15<sup>th</sup> May (f) 15<sup>th</sup> June.

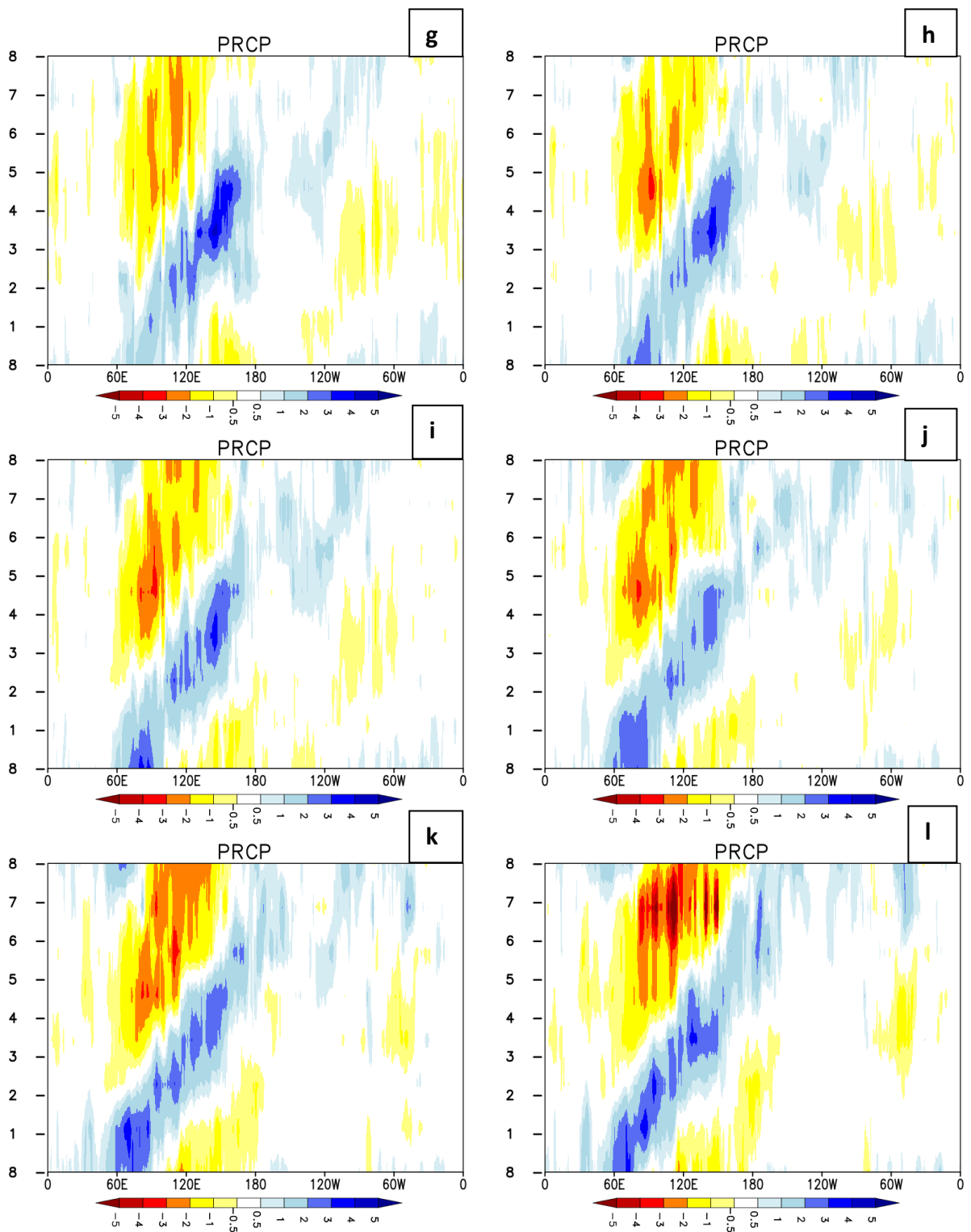


**Fig.13.** (continued) (g) 15<sup>th</sup> July (h) 15<sup>th</sup> Aug (i) 15<sup>th</sup> Sep (j) 15<sup>th</sup> Oct (k) 15<sup>th</sup> Nov (l) 15<sup>th</sup> Dec.

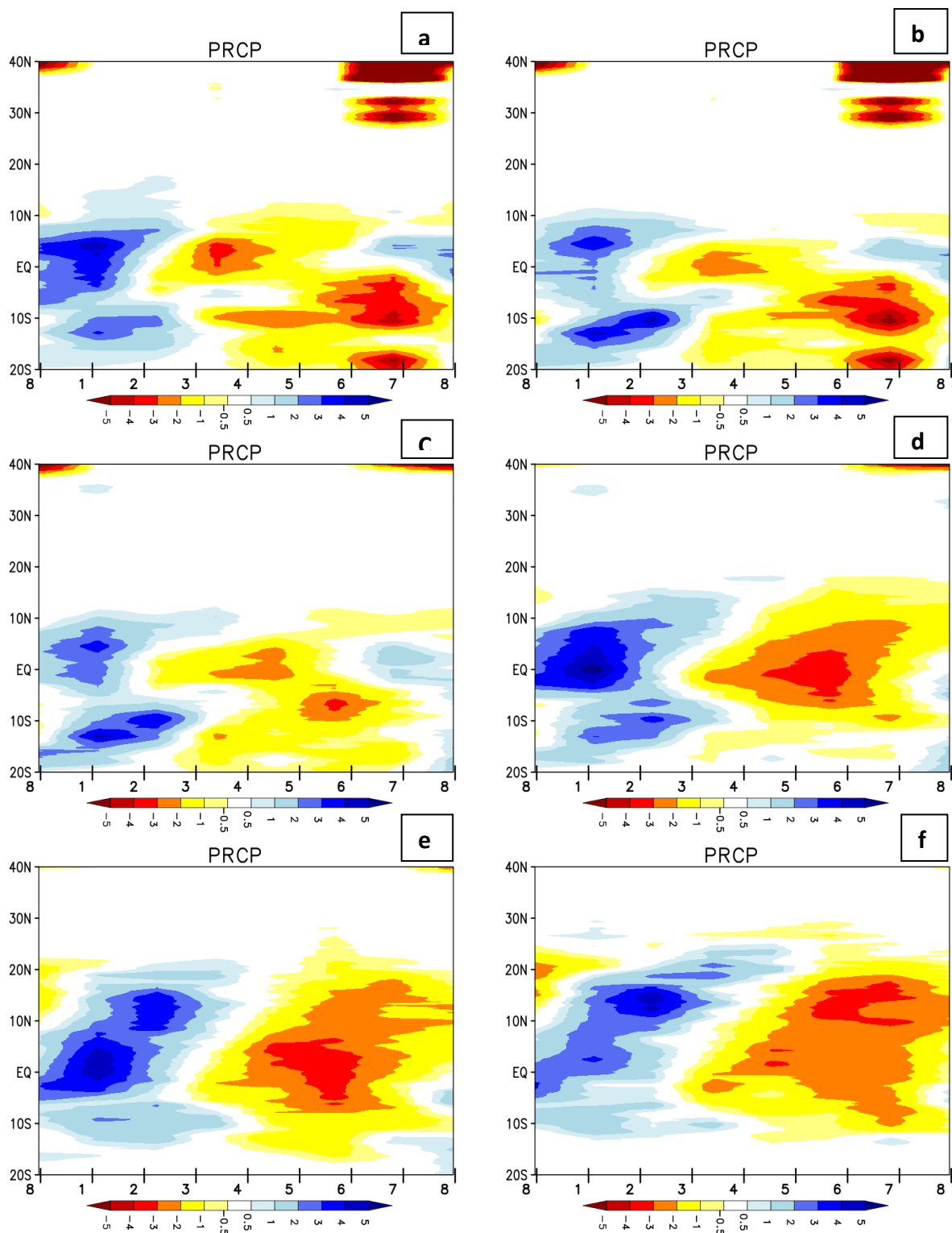


**Fig.14.** Hovmöller plots for precipitation anomalies (mm/day) to show northward propagation: (a) 15<sup>th</sup> Jan (b) 15<sup>th</sup> Feb (c) 15<sup>th</sup> Mar (d) 15<sup>th</sup> April (e) 15<sup>th</sup> May (f) 15<sup>th</sup> June.

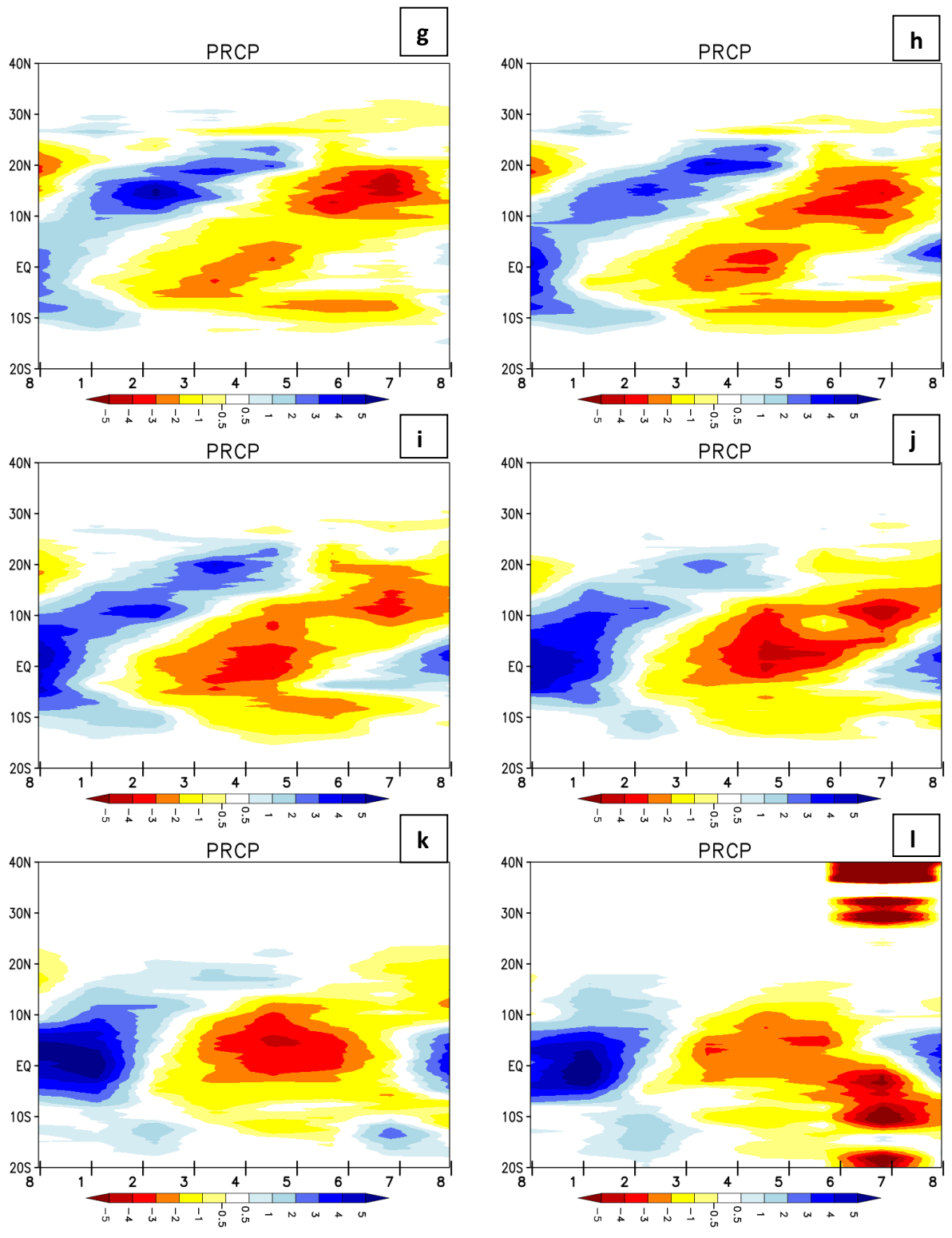


**Fig.14.** (continued) (g) 15<sup>th</sup> July (h) 15<sup>th</sup> Aug (i) 15<sup>th</sup> Sep (j) 15<sup>th</sup> Oct (k) 15<sup>th</sup> Nov (l) 15<sup>th</sup> Dec.

### MJO Filtered OLR anomalies (2013)

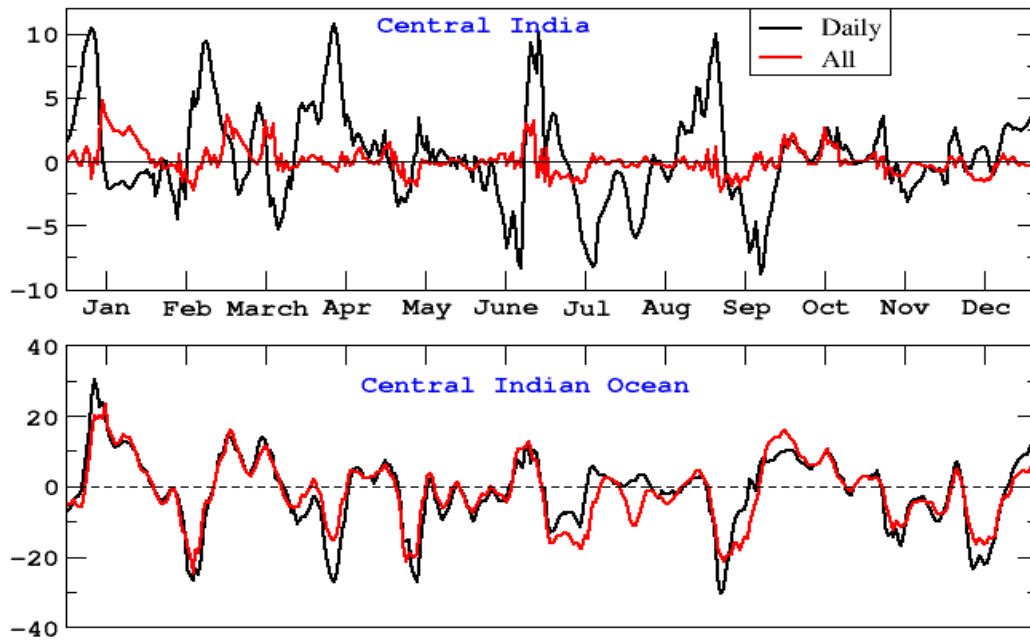
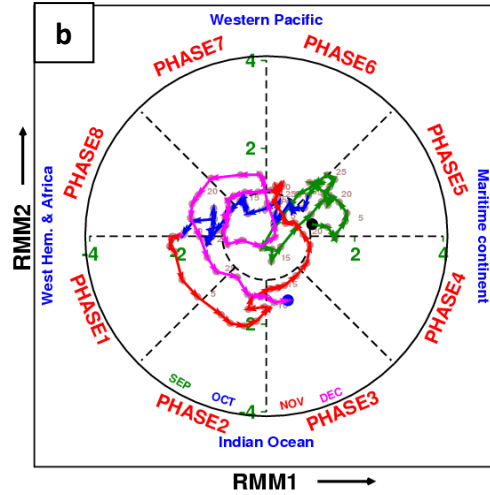
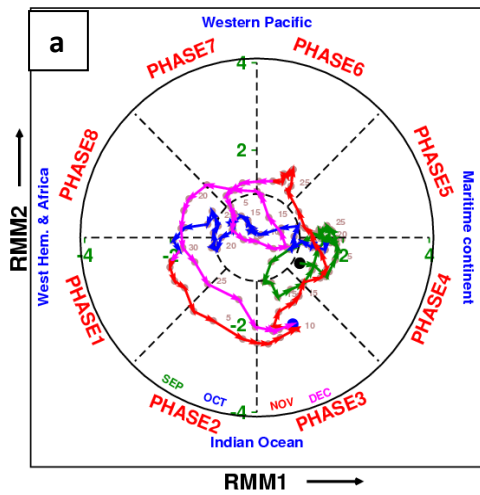
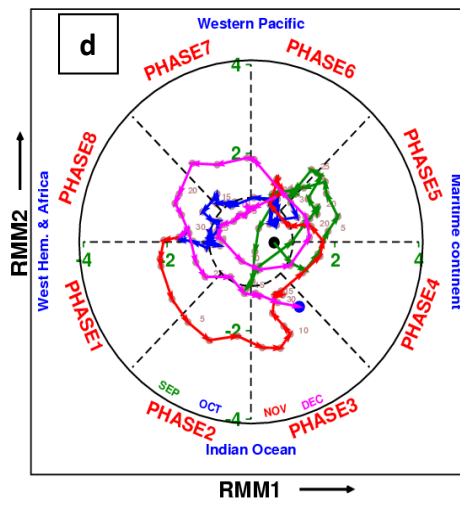
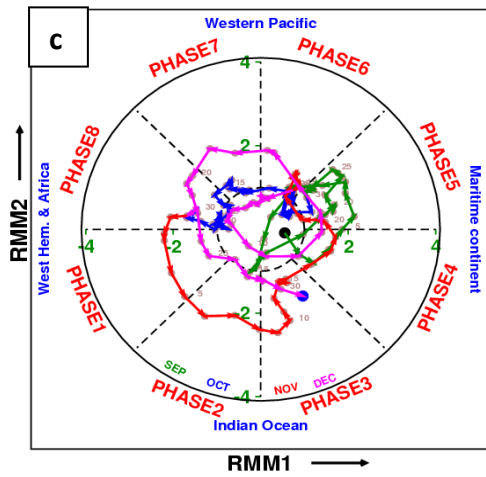


**Fig.15.** Reconstructed OLR anomalies over Central India and Indian Ocean. Black curve is based on lagged phase composite method (-45 day to +45 day, as discussed in Sec.4f) it takes seasonality into account and red curve is based on simple phase composite method (considering all the days of the year).



Real Time MJO monitoring of 2009 SEP OCT



Real Time MJO monitoring of 2009 SEP OCT

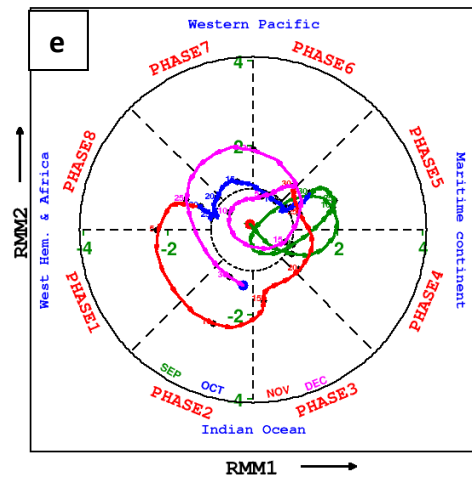


**Fig.16.**(PC1, PC2) phase space plot during 2009 SOND

- (a) Conventional WH method.
- (b) Same as Fig. 16(a) except Standardization of indices.
- (c) Same as Fig. 16(b) except Replacing OLR with Chi200.
- (d) Same as Fig. 16(c) except spatial averaging.
- (e) Same as Fig. 16(d) except with EEOF technique.

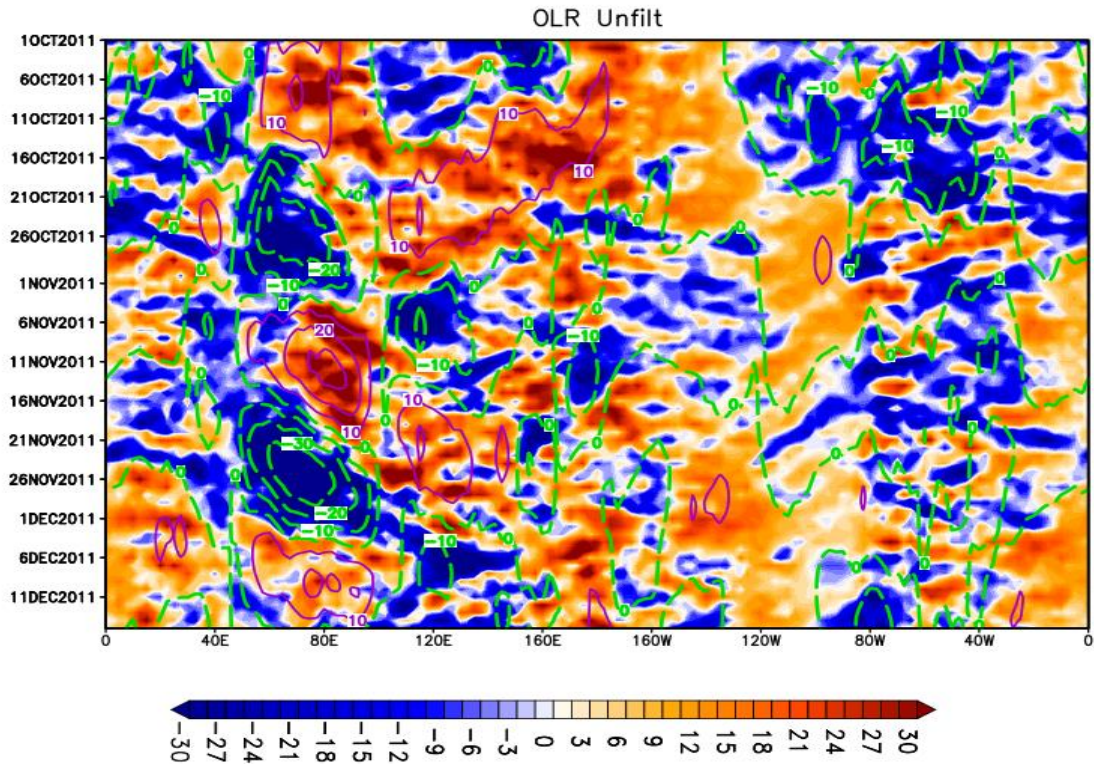


**Fig.17a.** Hovmoller plot of Unfiltered OLR anomaly (in  $W/m^2$ ; shaded), superimposed over it (contours) is the 20-90 day Lanczos filtered OLR anomaly during the DYNAMO period.

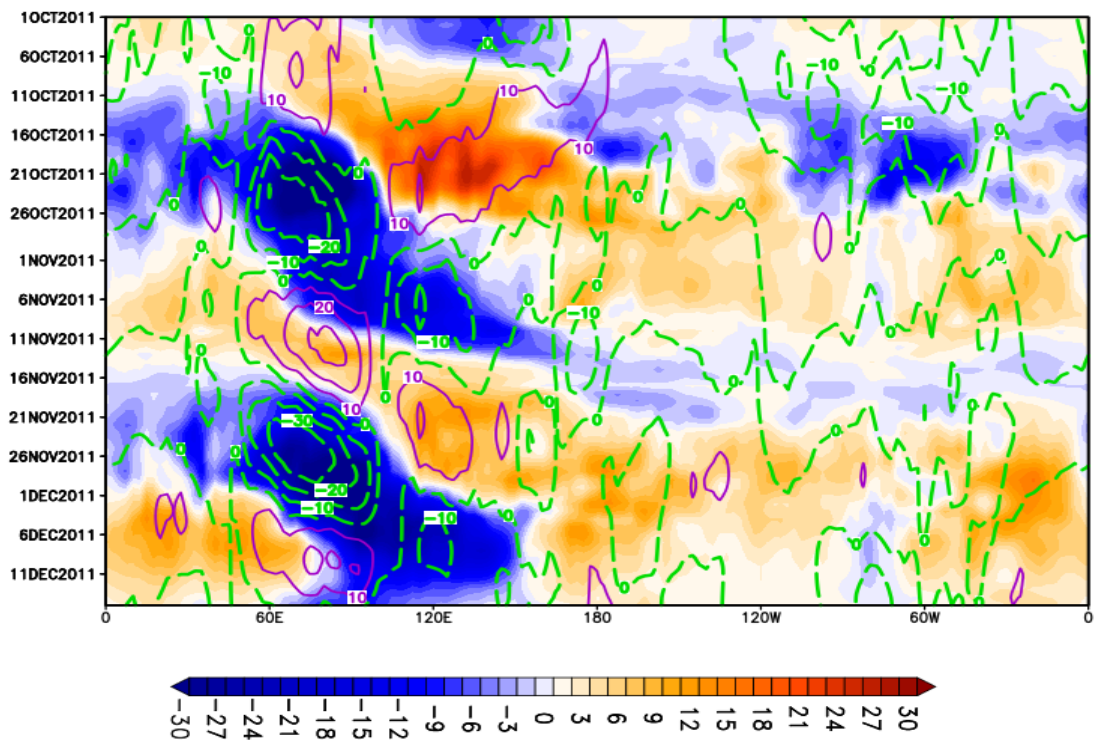


**Fig.17b.** Hovmoller plot of MJO filtered OLR (in  $W/m^2$ ; shaded), superimposed over it (contours) is the 20-90 day Lanczos filtered OLR anomalies during DYNAMO period.

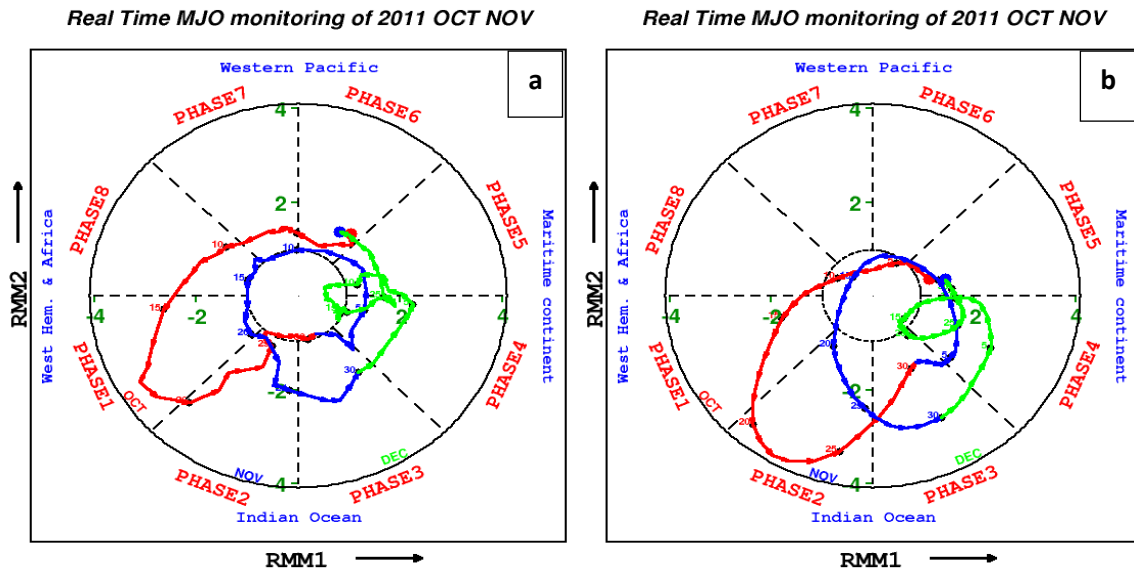


**Fig.18.** Comparison of MJO1 and MJO2 tracking during DYNAMO period (as discussed in Sec. 5b) based on (a) WH04 method (b) EEOF method.

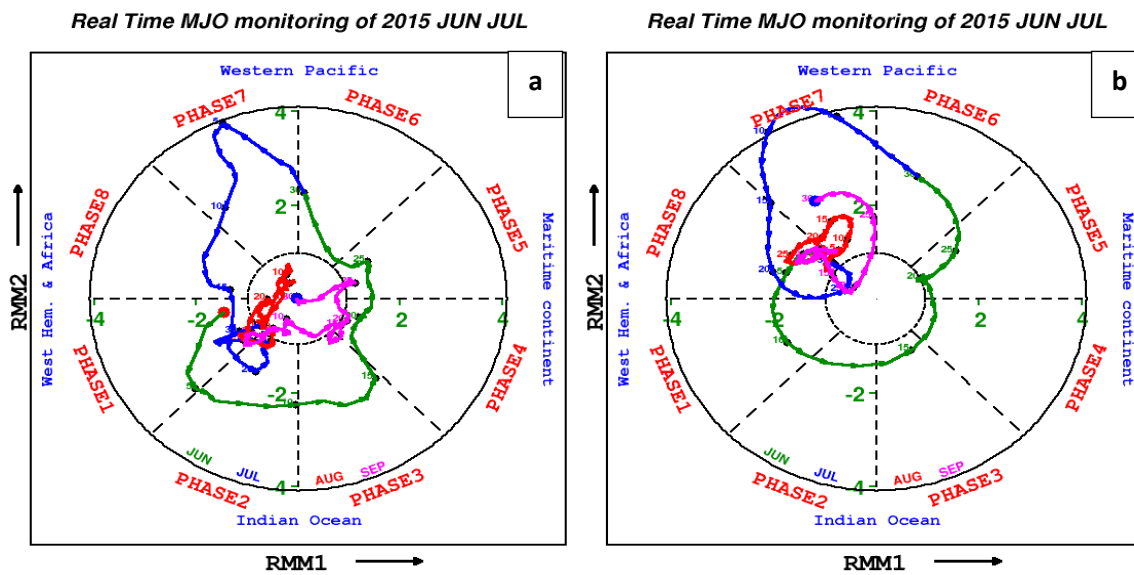


**Fig.19.** 2015 monsoon tracking based on (a) WH04 method and (b) EEOF method.

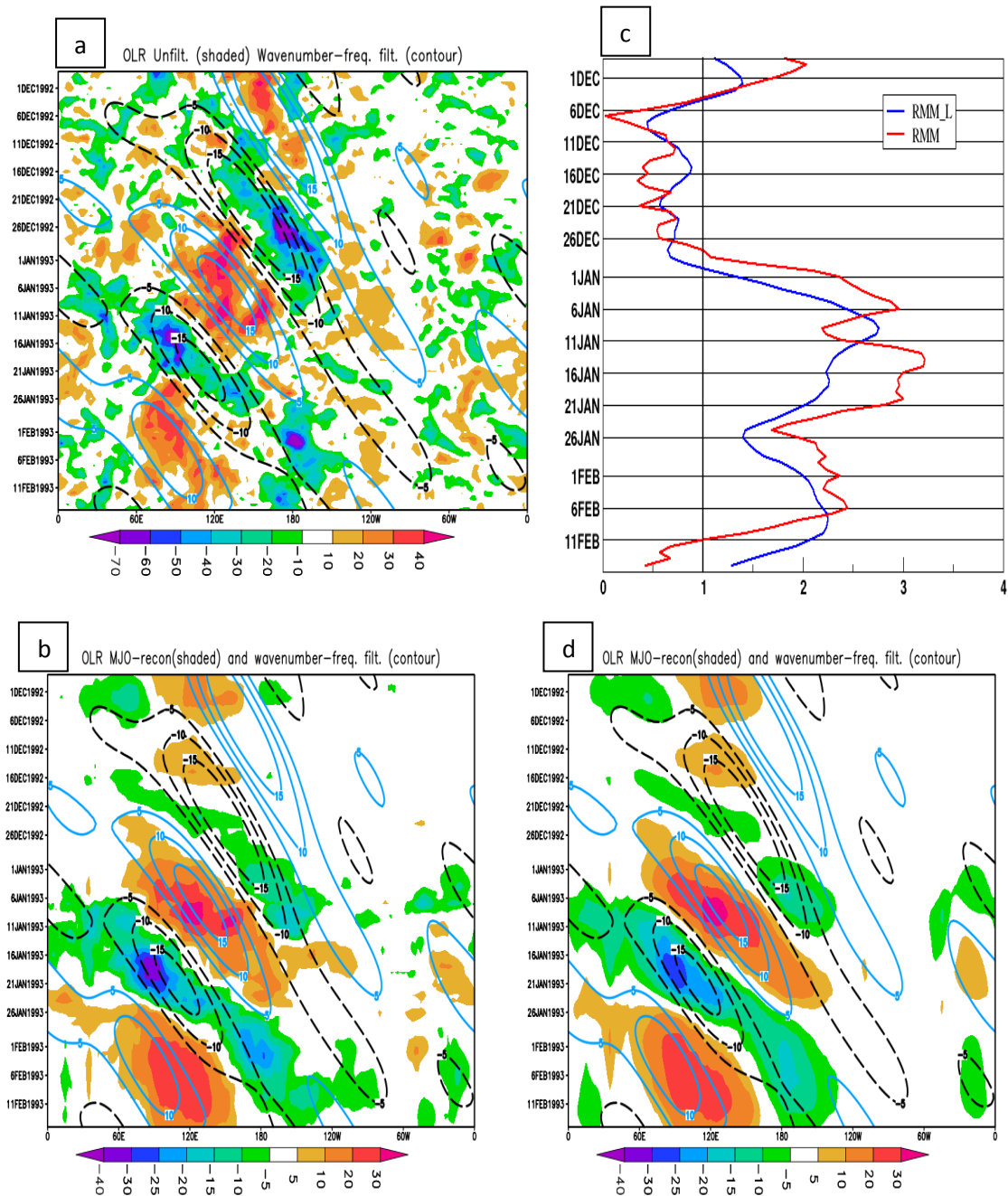
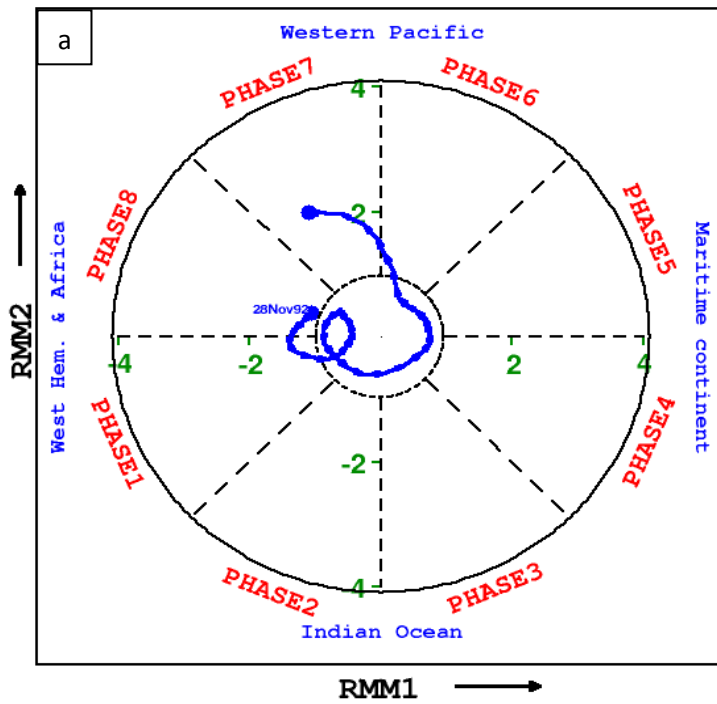


**FIG.20.**The two TOGA COARE MJO events between 28 Nov 1992 and 15 Feb 1993 represented by the RMM and RMM\_L for (a) raw OLR anomaly (in  $W/m^2$ ; shading) and filtered MJO (contour with interval  $5 W/m^2$  and 0 being omitted);(b) reconstructed anomalies (shaded) by RMM\_L and total filtered MJO [contour as in (a)]. (c) amplitudes of RMM (Red) and RMM\_L (blue);. Wave-number-Frequency filter in the range of wave number 1-5 and 20-100 day are used based on 2-D spectral decomposition as suggested by Wheeler and Kiladis (1999).(d) similar to fig. 20(b) except with regression based reconstruction.

Real Time MJO monitoring



Real Time MJO monitoring

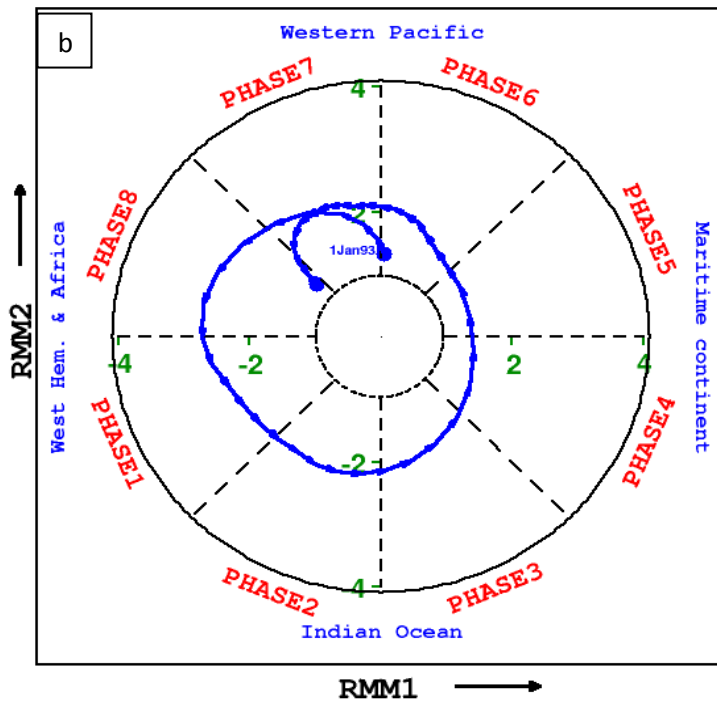
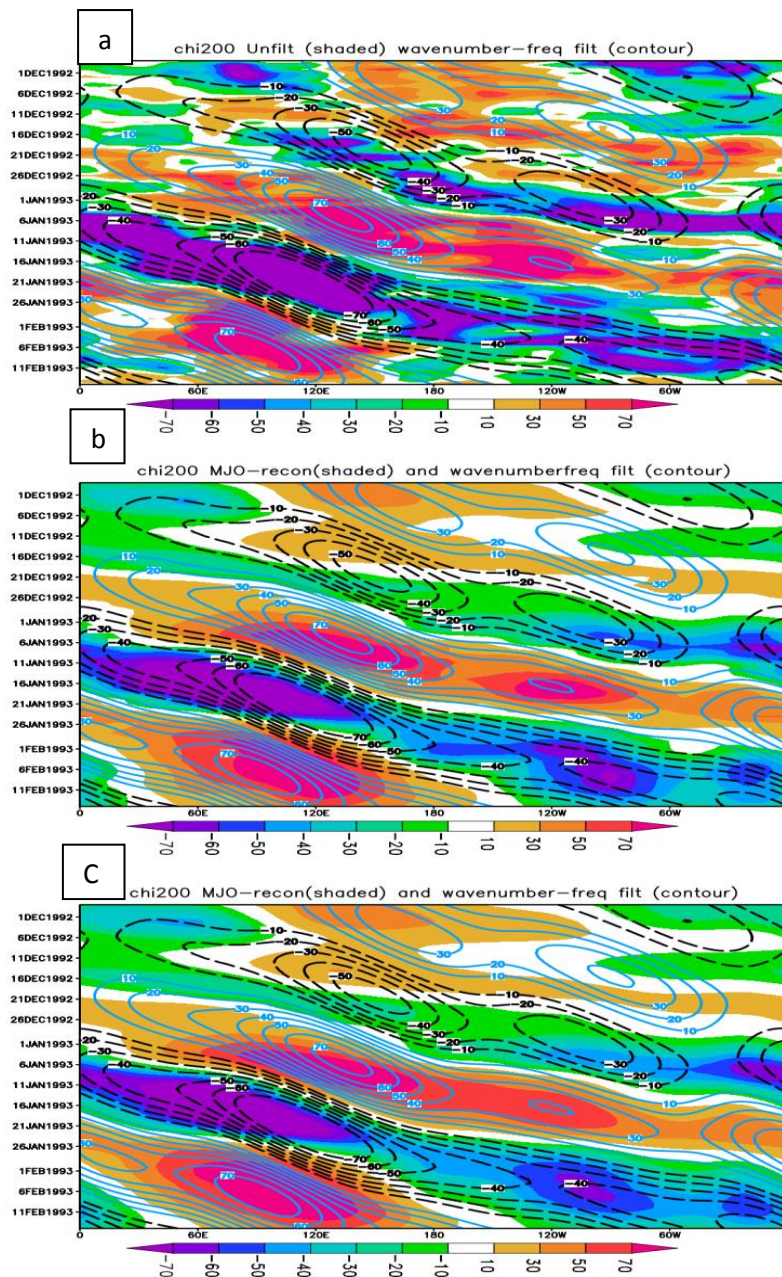
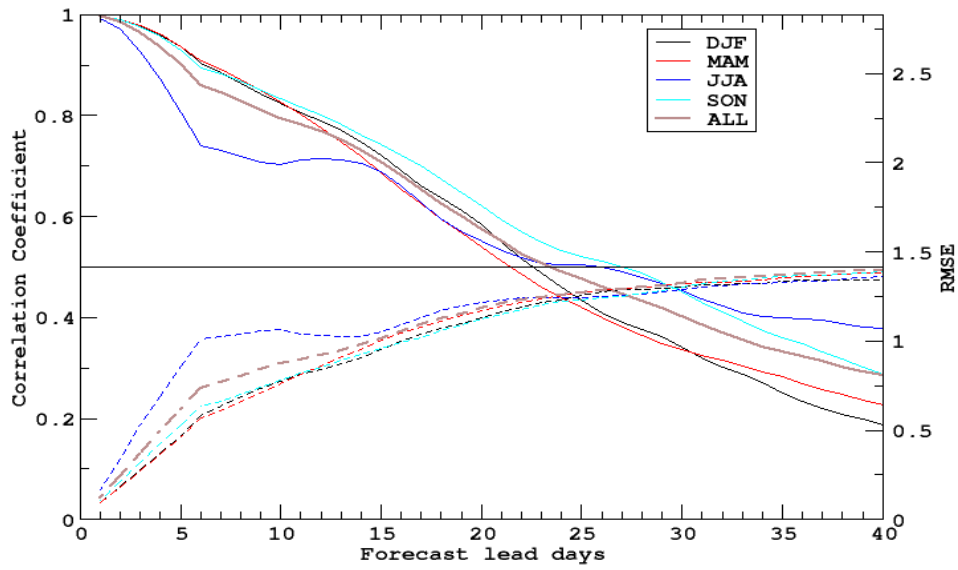


FIG.21. Cartesian phase diagrams following RMM\_L for the two events during TOGA COARE (a) 28 Nov 1992–5 Jan 1993 and (b) 1 Jan–15 Feb 1993.



**FIG.22.**(a) and (b) are same as Fig.20 (a) and (b) respectively, but for the velocity potential at 200hpa (chi200). (C)Same as Fig.20 (d) (i.e. based on regression based reconstruction) but for chi200. Contour with interval  $1 \times 10^5 \text{ m}^2/\text{s}$  and 0 being omitted, shaded regions are shown in  $10^5 \text{ m}^2/\text{s}$  units.



**Fig.23.** Season wise statistical skill of model during 2001-2010 CFSv2 Extended range hindcast periods. (Bivariate CC/RMSE)

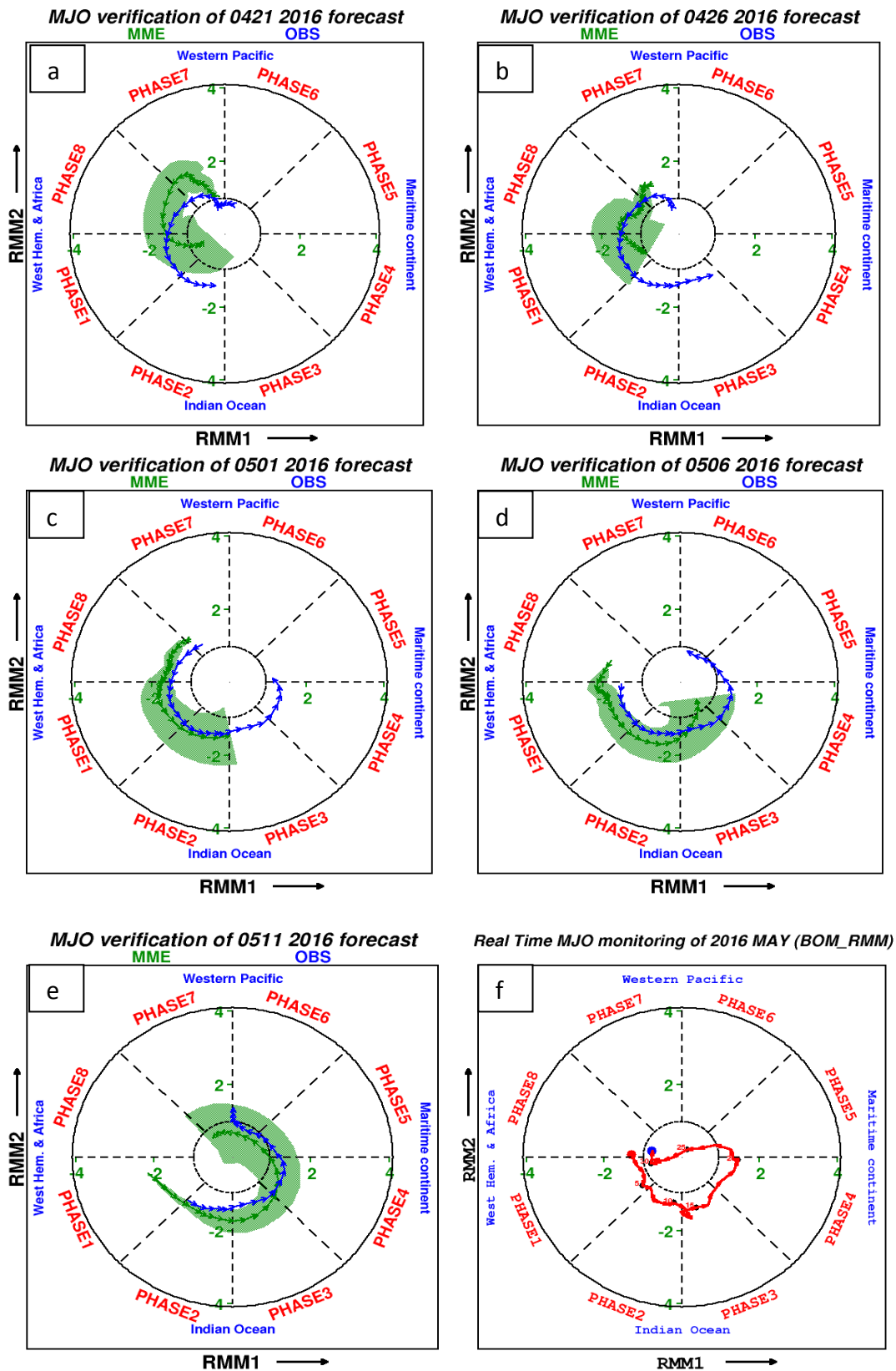


**Fig.24.** (PC1, PC2) phase space plot for next 25 days for MAY 2016 MJO event. Blue is for Observation and green is for the IITM extended range forecast. (a-e) are for different ICs (as mentioned in the title section of each fig.), (f) phase space plot of RMM index (obtained from Bureau of Meteorology) for MAY 2016.

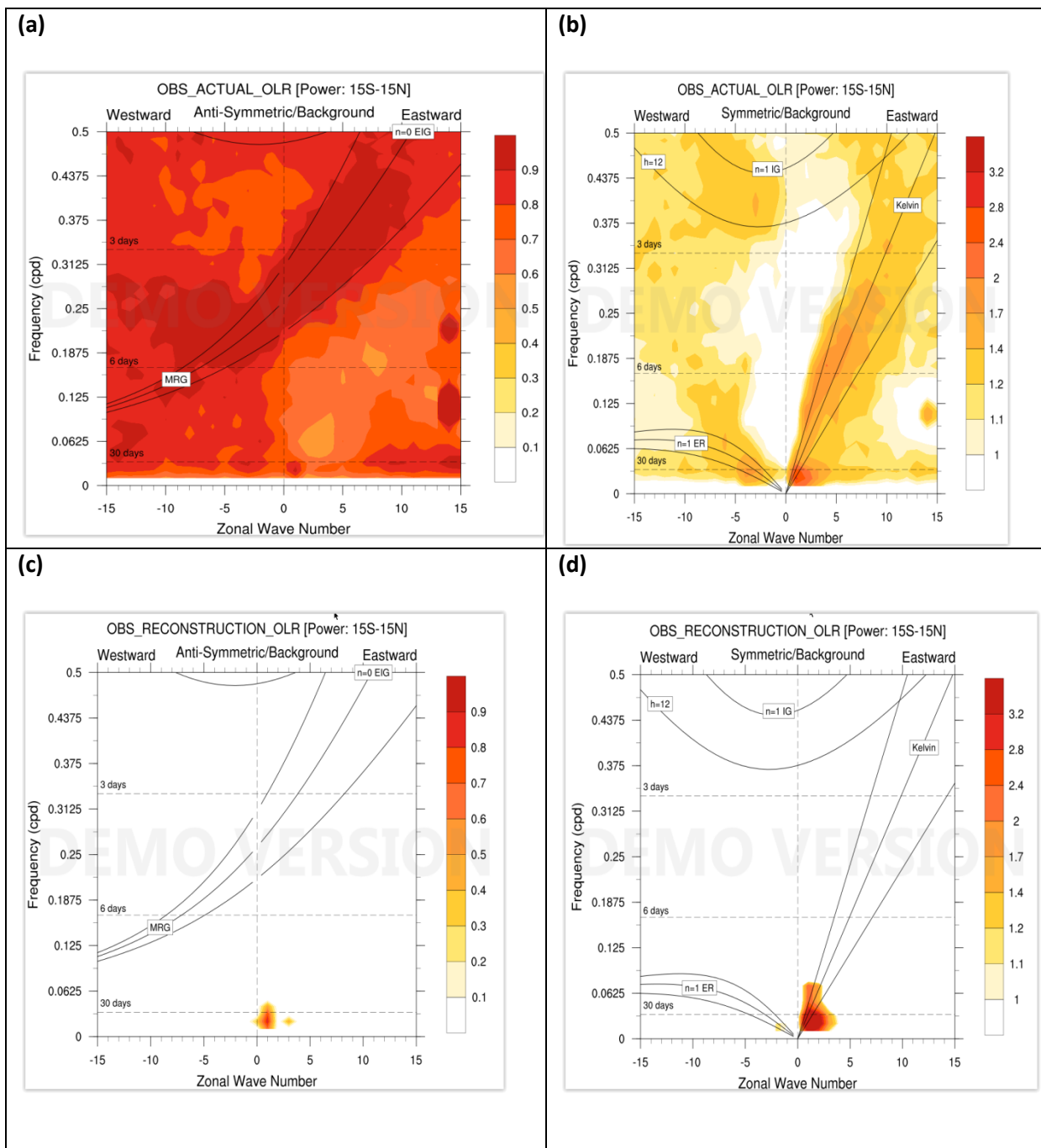


**Fig.25:** (a)-(b) Shows the space-time power spectra for the symmetric and the anti-symmetric part of actual OLR data (NOAA) averaged between 15°S-15°N. (c)-(d) shows the same but using the regression based OLR reconstruction (cf. Sec.4g). Power spectrum has the background removed as discussed in Wheeler and Kiladis (1999).